CrossMark

JM PAPERS

Effect of chemical reaction on mixing transition and turbulent statistics of cylindrical Richtmyer–Meshkov instability

Zheng Yan[1], Yaowei Fu[2,3], Lifeng Wang[1,4], Changping Yu[2] and Xinliang Li[2,3],†

[1]Institute of Applied Physics and Computational Mathematics, Beijing 100094, PR China

[2]LHD, Institute of Mechanics, Chinese Academy of Sciences, Beijing 100190, PR China

[3]School of Engineering Science, University of Chinese Academy of Sciences, Beijing 100049, PR China

[4]Center for Applied Physics and Technology, HEDPS, Peking University, Beijing 100871, PR China

Direct numerical simulations of a three-dimensional cylindrical Richtmyer–Meshkov instability with and without chemical reactions are carried out to explore the chemical reaction effects on the statistical characteristics of transition and turbulent mixing. We adopt 9-species and 19-reaction models of non-premixed hydrogen and oxygen separated by a multimode perturbed cylindrical interface. A new definition of mixing width suitable for a chemical reaction is introduced, and we investigate the spatio-temporal evolution of typical flow parameters within the mixing regions. After reshock with a fuller mixing of fuels and oxygen, the chemical reaction becomes sufficiently apparent at affecting the evolution of the flow fields. Because of the generation of a combustion wave within the combustion regions and propagation, the growth of the mixing width with a chemical reaction is accelerated, especially around the outer radius with large temperature gradient profiles. However, the viscous dissipation rate in the early stage of the chemical reaction is greater because of heat release, which results in weakened turbulent mixing within the mixing regions. We confirm that small-scale structures begin to develop after reshock and then decay over time. During the developing process, helicity also begins to develop, in addition to kinetic energy, viscous dissipation rate, enstrophy, etc. In the present numerical simulations with cylindrical geometry, the fluctuating flow fields evolve from quasi-two-dimensional perturbations, and the generations of helicity can capture this transition process. The weakened fluctuations during shock compression can be explained as the inverse energy cascade, and the chemical reaction can promote this inverse energy cascade process.

† Email address for correspondence: lixl@imech.ac.cn

1. Introduction

Richtmyer–Meshkov instability (RMI) widely exists in natural and engineering flows (Brouillette 2002; Zhou 2017*a*,*b*) such as supernova explosions(Almgren *et al.* 2006; Abarzhi *et al.* 2019), inertial confinement fusion (ICF) (Lindl *et al.* 2014; Wang *et al.* 2017*b*) and the interaction of a shock wave and a premixed or non-premixed flame (Billet 2005; Massa & Jha 2012; Attal & Ramaprabhu 2015; Jiang *et al.* 2016*a*). When a perturbed interface separating two fluids with different densities was accelerated by an incident shock wave, the perturbed interface developed gradually, experienced linear growth, nonlinear growth and finally a turbulent mixing, and this hydrodynamic instability has been termed as RMI (Richtmyer 1960; Meshkov 1969).

Richtmyer–Meshkov instability has been widely investigated theoretically (Dimotakis & Samtaney 2006; Vandenboomgaerde & Aymard 2011; Liu *et al.* 2014), experimentally (Motl *et al.* 2009; Zhai *et al.* 2010, 2012; Luo *et al.* 2014, 2015; McFarland *et al.* 2014; Zhai *et al.* 2018) and numerically (Lombardini, Pullin & Meiron 2012, 2014*a*,*b*; Zhou 2017*b*) over the past few decades for different geometries. Relative to classic planar geometry, Bell–Plesset (BP) effects are present in cylindrical or spherical geometries with increasing convergence effects (Bell 1951; Plesset 1954). The BP effects are reflected as additional perturbation growth from pure geometry, which leads to a more complex transition to turbulent mixing (Wang *et al.* 2013*b*, 2015). A large number of factors exist for the evolution of RMI, including initial conditions, Atwood numbers, Mach number, viscosity, etc. Random perturbations are always present on the interface in many practical engineering flows, which determines the eventual development of RMI (Thornber *et al.* 2010, 2017; Zhou 2017*b*; Zhou, Groom & Thornber 2020). The initial perturbations can be divided into single- and multi-mode perturbations, depending on the perturbed modes. For the multi-mode perturbation, the initial narrowband and broadband perturbed modes correspond to different growth rates via the physical processes of mode couplings and competitions, respectively. The broadband perturbed modes lead to a faster growth rate, which is more consistent with laser experiments (Thornber *et al.* 2010; Groom & Thornber 2020). Different combinations of mixing materials can be summarized as the Atwood number effect, which describes the growth-reduction mechanism for the diffusion (Lombardini *et al.* 2011). With the increase of the Atwood number, the asymmetry of bubbles and spikes becomes more and more apparent. Mach number effects might be controversial. With the increase of the initial Mach numbers, the scale separations would increase via increasing the perturbed velocity. However, the mixing parameter, the growth of the internal scale and the decaying rates of kinetic energy and enstrophy are found to be independent of the initial Mach numbers (Lombardini *et al.* 2012; Tritschler *et al.* 2014).

In extreme circumstances, chemical or nuclear reactions exist because of the high temperature, and the reactive instability could be classified into Rayleigh–Taylor instability (RTI) and RMI. The heat release within chemical reaction regions can change the thermodynamic parameters of flow fields and affect the temporal evolutions of RMI and RTI (Zhou *et al.* 2019, 2021). The reactive RMI is of central importance in Scramjet engines, multiphase combustion in propulsion applications and dust cloud explosions like coal mines and food processing facilities. In Scramjet applications the enhanced mixing by RMI assures sufficient combustion within the residence times. The reactive RTI also applies in ultra-compact combustors in gas turbine systems, ICF and type Ia supernovae explosions (Chertkov, Lebedev & Vladimirova 2009; Zhou *et al.* 2021).

The combustion can be divided into premixed and non-premixed. For premixed combustion, the interactions of shock waves and perturbed flames are the core issues in reactive RMI, which originate from the heat release effect because of a chemical reaction.

Under the effect of shock wave propagation, the heat release rates can increase nearly 30 times with the interactions of an inclined shock wave and a sinusoidally perturbed flame (Khokhlov *et al.* 1999). Kilchyk, Nalim & Merkle (2011) noted that the fuel consumption rate of a premixed laminar flame increased rapidly, which was dominated by a one-dimensional shock compression effect. For chemical reaction effects on the evolution of perturbed interfaces, Massa & Jha (2012) employed the linear stability method to explore the evolution of a premixed flame with a single shock and concluded that the growth of small-scale perturbations can be suppressed by chemical reactions, which results from baroclinic effects. Jiang *et al.* (2016*a*) hypothesized two time scales for the evolution of a perturbed interface. One is the time scale for chemical reactions, and the other is the time scale for RMI. They confirmed that the time scale for RMI is dominant in the early stage, and the time scale for a chemical reaction is dominant in the late stage. Later, Jiang, Dong & Wu (2016*b*) studied the multiple interactions of a flame interface with an incident shock wave to explore the effects of different initial perturbed amplitudes and thought that large amplitudes of the initial perturbed interface lead to large-scale vortex structures before the passages of reshock waves, which results in quick growth of the perturbed interface. After the successive impacts of multiple reshock waves, the chemical reaction weakens the baroclinic torque and begins to dominate, in contrast with the initial perturbed amplitudes.

In contrast to premixed combustion, non-premixed combustion is more challenging in experimental studies and engineering applications because of the difficulty of initial ignition and the uncertainty of chemical kinetic mechanisms (Zhou *et al.* 2021). However, benefiting from the developments of numerical simulations, important progress exists to uncover the intrinsic physical process of non-premixed combustion. Attal & Ramaprabhu (2015) carried out two-dimensional numerical simulations of a single-mode chemical reacting RMI with hydrogen (H_2) and oxygen (O_2) at different sinusoidal interface thicknesses, and the combustion waves impulsively accelerated any material line to promote the growth of the perturbed interfaces. Later, they also added the methane–air chemistry into an astrophysical code (FLASH) (Attal *et al.* 2015). Bambauer, Hasslberger & Klein (2020) carried out three-dimensional direct numerical simulations (DNS) of reactive RMI in plane geometry with multimodal initial perturbations, and found that the flame surface area is reduced by 50 %. Due to high computational costs, the detailed chemistry is not considered. Later, Bambauer *et al.* (2021) investigated the vortex dynamics and fractal structures in reactive RMI, and confirmed that baroclinic torque is dominant during shock-flame interactions. The interactions of the incident shock wave and combustion waves would result in non-planarity effects from combined RTI and RMI actions (Attal & Ramaprabhu 2015; Zhou 2017*a*). Nevertheless, few works have focused on the chemical reaction effects on mixing transition and turbulent statistics with detailed chemistry in three-dimensional numerical simulations, especially within the frame of cylindrical or spherical geometries. The curved geometry is widely at present in the applications of ICF, supernova collapse and explosive detonations (Lombardini *et al.* 2014*a*; Zhou 2017*b*). Hence, in this paper we select the cylindrical shock wave and perturbed interface to carry out DNS of RMI with and without chemical reactions and uncover the statistical characteristics during the process of transition and late-time turbulent mixing.

The rest of the paper is organized as follows. In § 2 we introduce the detailed computational settings, including the governing equations, initial conditions and chemical reactions. Next, in § 3 the numerical results are presented, and we discuss the shock propagation, grid resolution, mixing width and other turbulent statistics. The conclusions are summarized in § 4.

2. Numerical settings

We perform DNS of RMI with and without chemical reactions using our open-source software Opencfd-Comb. A sixth-order finite difference scheme (OMP6) (Li, Leng & He 2013) is adopted to discretize the convective terms, and an eighth-order central difference scheme is adopted to discretize the viscous terms. In addition, we employ the standard third-order Runge–Kutta method as the time-marching scheme. The software Opencfd-Comb has been widely validated in our previous work, including supersonic jet flows (Fu *et al.* 2019*a*,*b*) and RMI (Fu, Yu & Li 2020; Li *et al.* 2021).

2.1. *Governing equations*

The conservation form of three-dimensional compressible Navier–Stokes equations with multi-species of miscible gases reads as

$$\frac{\partial \rho}{\partial t} + \nabla \cdot (\rho \boldsymbol{u}) = 0, \tag{2.1a}$$

$$\frac{\partial \rho \boldsymbol{u}}{\partial t} + \nabla \cdot (\rho \boldsymbol{u}\boldsymbol{u}) = -\nabla (p\boldsymbol{\delta} - \boldsymbol{\sigma}), \tag{2.1b}$$

$$\frac{\partial E}{\partial t} + \nabla \cdot (\rho (E + p) \boldsymbol{u}) = \nabla (\boldsymbol{\sigma} \cdot \boldsymbol{u} + \boldsymbol{q}) + Q_s, \tag{2.1c}$$

$$\frac{\partial \rho Y_m}{\partial t} + \nabla \cdot (\rho Y_m \boldsymbol{u}) = \nabla \cdot (\rho D_m \nabla Y_m) + \dot{W}_m, \tag{2.1d}$$

where ρ denotes the mixture density, $\boldsymbol{u}$ denotes the velocity vector, p is the static pressure, $\boldsymbol{\delta}$ is the Kronecker function and Y_m is the mass fraction of the mth species of mixture. Here E is the total energy per unit volume, which is defined as

$$E = \frac{1}{2}\rho \boldsymbol{u}^2 + \sum_{m=1}^{N} \rho_m h_m - p, \tag{2.2}$$

where N denotes the total number of reactive species, ρ_m is the mth-species density and h_m is the mth-species enthalpy. According to Stokes' hypothesis, the bulk viscosity is assumed to be zero (Graves & Argrow 1999), and the viscous stress tensor $\boldsymbol{\sigma}$ for a Newtonian fluid is defined as

$$\sigma_{ij} = \mu \left(\frac{\partial u_i}{\partial x_j} + \frac{\partial u_j}{\partial x_i} - \frac{2}{3}\theta \delta_{ij} \right), \tag{2.3}$$

where $\theta = \partial u_k / \partial x_k$ corresponds to the compression or expansion of fluid elements and μ is the mixture viscosity. According to Fourier's law and Fick's law, the conductive heat flux $\boldsymbol{q}$ is given as

$$\boldsymbol{q} = \kappa \nabla T + \rho \sum_{m=1}^{N} D_m h_m \nabla Y_m, \tag{2.4}$$

where κ is the thermal conductivity of the mixture, T is the temperature of the mixture and D_m is the mth-species effective binary diffusion coefficient. Here Q_s $(\mathrm{J\,(m^3\,s)^{-1}})$ is

941 A55-4

the heat release rate per unit volume for the chemical reaction, which can be computed by

$$Q_s = - \sum_{m=1}^{N} \dot{W}_m h_m^0, \tag{2.5}$$

where h_m^0 represents the mth-species enthalpy production rate per unit mass and $\dot{W}_m$ represents the mass production rate per unit volume. According to the Dalton's law of partial pressures and the isothermal hypothesis, the equation of state can be expressed as

$$p = \sum_{m=1}^{N} \rho_m R_m T = \sum_{m=1}^{N} \rho_m \frac{R_0}{M_m} T, \tag{2.6}$$

where $R_0 = 8.314 \,\mathrm{J\,(mol\,K)}^{-1}$ is the universal gas constant and M_m is the mth-species molar mass. Hence, the molarity can be defined as $[X_m] = \rho_m / M_m$. The specific heat at constant pressure per unit mass C_p, enthalpy per unit mass h and entropy S per unit mass are computed through the following fitting polynomials (Gordon & McBride 1971):

$$\frac{C_{p_m}}{R_m} = A_m + B_m T + C_m T^2 + D_m T^3 + E_m T^4, \tag{2.7a}$$

$$\frac{h_m}{R_m} = A_m T + \frac{1}{2}B_m T^2 + \frac{1}{3}C_m T^3 + \frac{1}{4}D_m T^4 + \frac{1}{5}E_m T^5 + F_m, \tag{2.7b}$$

$$\frac{S_m}{R_m} = A_m \ln T + B_m T + \frac{1}{2}C_m T^2 + \frac{1}{3}D_m T^3 + \frac{1}{4}E_m T^4 + G_m. \tag{2.7c}$$

Here $A_m, B_m, C_m, D_m, E_m, F_m, G_m$ are the corresponding fitting coefficients and $h_m^0 = R_m F_m$. Hence, the specific heat at a constant pressure of the mixture $C_{p_{mix}}$ and the mixture enthalpy h_{mix} can be computed through

$$C_{p_{mix}} = \sum_{m=1}^{N} C_{p_m} Y_m, \quad h_{mix} = \sum_{m=1}^{N} h_m Y_m. \tag{2.8a,b}$$

The mth-species viscosity μ_m, thermal conductivity κ_m and effective binary diffusion coefficient D_m can be computed by fitting polynomials from *CHEMKIN* (Kee, Rupley & Miller 1989). Therefore, the mixture viscosity μ and the thermal conductivity of the mixture κ can be obtained by

$$\mu = \sum_{m=1}^{N} \frac{X_m \mu_m}{\sum_{j=1}^{K} X_j \Phi_{mj}}, \quad \kappa = \frac{1}{2}\left(\sum_{m=1}^{N} X_m \kappa_m + \frac{1}{\sum_{m=1}^{N} X_m/\kappa_m}\right). \tag{2.9a,b}$$

Here,

$$\Phi_{mj} = \frac{1}{\sqrt{8}}\left(1 + \frac{M_m}{M_j}\right)^{-1/2}\left[1 + \left(\frac{\mu_m}{\mu_j}\right)^{1/2}\left(\frac{M_j}{M_k}\right)^{1/4}\right]^2. \tag{2.10}$$

In addition, the mth-species effective binary diffusion coefficient D_m can be obtained by

$$D_m = \frac{1 - X_m}{\sum_{j=1, j \neq m}^{N} X_j / D_{jm}}, \tag{2.11}$$

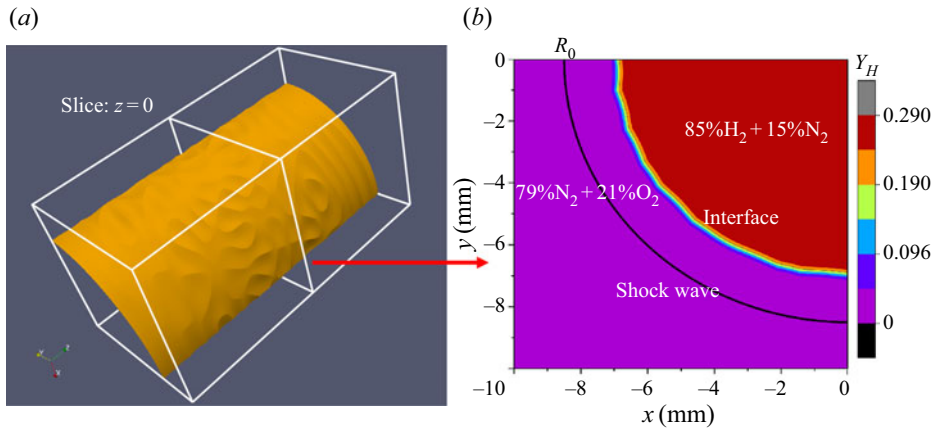where X_m is the mth-species volume fraction.

Figure 1. (*a*) Isosurface of the mass fraction of hydrogen Y_H with 5 % at the initial status. (*b*) Contour slice of the mass fraction of hydrogen Y_H at the cross-section of $z = 0$, and the black convergent curve denotes the position of the shock wave.

2.2. *Initial condition*

Consistent with our previous work (Fu *et al.* 2020), we employ the multimode initial interfacial perturbation proposed by Lombardini *et al.* (2014*a*). Although the initial condition effects are crucial for nonlinear growth or late-time fully developed turbulent flows (Budzinski, Benjamin & Jacobs 1994; Youngs 2013; Vandenboomgaerde *et al.* 2014), the initial conditions of the two cases we carried out in this paper are the same. Hence, we just ignore the initial condition effects and focus on the effect of a chemical reaction.

The perturbed surface separating fluids with different densities are defined as $r = \zeta_0(\theta, \phi)$, and the mass fraction field $\psi(r, \theta, \phi)$ can be obtained by

$$\psi(r, \theta, \phi) = \frac{1}{2} \left\{ 1 - \tanh \left[\frac{r - \zeta_0(\theta, \phi)}{L_r} \right] \right\}, \tag{2.12}$$

where $\zeta_0(\theta, \phi) = R_0 - a_0|f(R_0, \theta, \phi)|$, $f(R_0, \theta, \phi) = \sum_{l=0}^{M} \sum_{m=-l}^{l} f_{lm} Y_{lm}(\theta, \phi)$, $f_{lm} = \sqrt{(2l+1)C_l} \cos(2\pi\omega_l^m) / \sqrt{\sum_{i=-l}^{l} \cos(2\pi\omega_l^i)}$. For more detailed definitions, we refer the reader to Lombardini *et al.* (2014*a*) and Fu *et al.* (2020). Our main computational domain is $L_x \times L_y \times L_z = 20 \, \text{mm} \times 20 \, \text{mm} \times 20 \, \text{mm}$ with a homogeneous Cartesian mesh. We set up periodical boundary conditions for the z direction, and buffer regions are adjoined to the main computational domain in the x and y directions with a sparse mesh to avoid the effect of shock reflection at the boundary. The grid resolution in the main computational domain is 1024^3. For the initial perturbed interface, we set the position located at $R_0 = 7$ mm, the characteristic thickness $L_r = 0.2$ mm, the dominant spherical wavenumber $l_0 = 20$, the variance $\sigma_0 = l_0/15$ and $a_0 = 0.375$ mm.

We show the isosurface of the mass fraction of hydrogen Y_H with 5 % at the initial status in figure 1(*a*), and only a quadrant is selected to exhibit the perturbed interface. To further demonstrate the multi-mode characteristics, a contour slice at the cross-section of $z = 0$ is shown in figure 1(*b*). A perturbed interface with a characteristic thickness is apparent, which assures the development of late-time turbulent mixing.

To be consistent with the one-dimensional shock tube experiment (Vetter & Sturtevant 1995; Leinov *et al.* 2009) and other numerous simulations (Hill, Pantano & Pullin 2006; Lombardini *et al.* 2011; Bengoechea *et al.* 2014), an initial convergent shock Mach number

	Pre-shock		Post-shock
	85 % H_2 and 15 % N_2	79 % N_2 and 21 % O_2	79 % N_2 and 21 % O_2
P (Pa)	101 325	101 325	246 047.8
ρ (Kg m^{-3})	0.08988	0.4393	0.8390
U_r (m s^{-1})	0	0	396.102

Table 1. Flow parameters at the initial status; U_r is the radial velocity.

is set as $M_s = 1.5$ with the position of $R_s = 8.5$ mm. The inner species of the perturbed cylinder are full of 85 % H_2 and 15 % N_2, with a pressure of 101 325 Pa and a temperature of 800 K. The outer species of the perturbed cylinder are full of 79 % N_2 and 21 % O_2, and their pressure and temperature are the same as those of the inner species. Other thermal variables and the velocity vector can be computed according to the Rankine–Hugoniot condition (Anderson 2010), and they are listed in the table 1.

2.3. *Chemical reaction computations*

In our numerical simulations we adopted an updated 9-species (H_2, H, O_2, O, OH, HO_2, H_2O_2, H_2O and N_2) and 19-reaction model proposed by Li *et al.* (2004). The kinetic model of the H_2/O_2 reaction can be written uniformly as

$$\sum_{i=1}^{9} v_{ij}B_i \rightleftharpoons \sum_{i=1}^{9} v'_{ij}B_i, \quad (j = 1, 2, \ldots, 19), \tag{2.13}$$

where B_i denotes the ith species and v_{ij} and v'_{ij} are stoichiometric numbers of reactants and products, respectively. The mass production rate of the ith species because of the jth chemical reaction can be computed as

$$\left(\frac{d\rho_i}{dt}\right)_j = M_i \left(v'_{ij} - v_{ij}\right) \left(\eta_j - \eta'_j\right). \tag{2.14}$$

Here, η_j denotes the forward reaction rate, which is computed from the Arrhenius formula; η'_j denotes the reversal reaction rate, which needs to involve the chemical equilibrium constant. Therefore, the mass production rate for the ith species is obtained by summing all element reactions,

$$\dot{W}_i = \sum_{j=1}^{N} \left(\frac{d\rho_i}{dt}\right). \tag{2.15}$$

3. Results and discussions

3.1. *Shock propagation*

According to Guderly's theory, there exists a similarity exponent α to bridge a connection of the strong shock position $R_s(t)$ and propagation time t as $R_s(t) \sim (1 - t/t_s)^\alpha$ (Guderley 1942), and t_s is the time when a strong shock reaches the origin. The similarity exponent can be obtained by solving ordinary differential equations, and it depends on the ratio of specific heat for cylinder geometry (Dyke & Guttmann 1982; Chisnell 1998; Lombardini
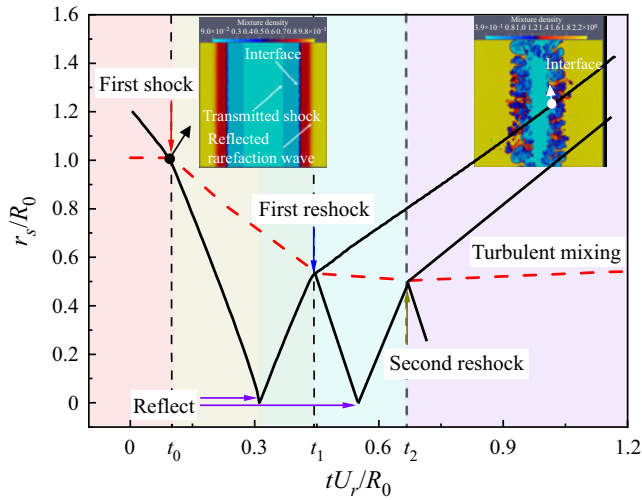
Figure 2. Diagram of shock propagation, with first shock, reflection, reshock and turbulent mixing. Here r_s denotes the positions of the shock wave (solid black line) and the inner radius of the mixing regions (dashed red line). The insets are two-dimensional contour slices of the mixture density without a chemical reaction. Their instants are after the first shock and eventual mixing.

& Pullin 2009). In our numerical simulations with or without chemical reactions, the fitted slopes are 0.800, which is consistent with the theoretical prediction.

The shock propagation diagram shown in figure 2 provides an abundant physical configuration of the temporal evolutions of cylindrical RMI. Over time, the strong shock propagates to the origin convergently. The speed of shock propagation is not constant, although the curve in figure 2 seems to be straight visually. After the first interaction of the incident shock and perturbed interface (t_0), a transmitted shock propagating to the origin and a reflected expansion wave propagating outwardly are produced, and the perturbed interface accelerates inwardly. The reflected expansion wave propagates divergently to the boundary, and its propagation time in coarse grids is long enough to avoid pollution on the flow field in our numerical simulations. The transmitted shock converges to the origin and then reflects at the origin outwardly. Subsequently, the interaction of the shock wave and perturbed interface reoccurs, and the acceleration direction of the perturbed interface is reversed. The light-to-heavy fashion would generate a transmitted shock propagating outwardly and a reflected shock propagating inwardly (Lombardini *et al.* 2014a). After the first reshock (t_1), the fluid instability would develop quickly, along with transition and turbulent mixing. Sufficient mixing is needed for an apparent chemical reaction, and the instant of the first reshock is marked as the starting time for the apparent chemical reaction effect. During the process of shock propagating within the mixing regions, the velocity fluctuations would be weakened, which is represented by the smaller turbulent kinetic energy, the smaller enstrophy, the smaller palinstrophy and the smaller viscous dissipation rates. In addition, the weakened fluctuations are also reflected by the inverse energy cascade process. The specific discussions are exhibited in the later sections in detail. The same shock propagation diagram is repeated after the first reshock, but the shock strength is smaller over time. In our numerical simulations and temporal analysis, we focus on the temporal ranges from the instant before the first reshock and the instant after the second reshock (t_2) to uncover the physical configurations of the perturbed interface, and they are marked up with a background colour of light cyan and purple in the subsequent figures.

The diagram of the shock propagation with a chemical reaction is much the same as the case without a chemical reaction. Their diagrams of shock propagation are similar to the classic RMI with cylinder geometry in numerical simulations (Hill *et al.* 2006; Lombardini *et al.* 2011; Wu, Liu & Xiao 2021) and experiments (Houas & Chemouni 1996; Si *et al.* 2015; Ding *et al.* 2019). Because of the complex definition of the mixing width involved in a chemical reaction, the interface motion will be discussed in detail in the subsequent section.

3.2. *Grid resolution*

The criteria for transition to turbulent mixing have always been an indeterminate issue for RMI for a long time, and the transition criteria involve spatial and temporal scales of large separations (Zhou *et al.* 2003; Zhou 2007, 2017*a*). Turbulent mixing means rapid mixing of momentum and concentration at the molecular scale (Dimotakis 2000), which is beneficial to a chemical reaction. After reshock, the flow quickly tends to transition to a turbulent state (Tomkins *et al.* 2013). Hence, we may select the time after the reshock as turbulent mixing from the perspective of temporal criteria. For spatial criteria, we focus on the characteristic length scales (Taylor microscale λ and Kolmogorov viscous scale η) to evaluate whether the flow has developed a turbulent field (Cook & Zhou 2002; Yan *et al.* 2019). Their definitions are

$$\lambda_r = \left[\frac{\langle u_r^2 \rangle}{\langle (\partial u_r / \partial x_r)^2 \rangle} \right]^{1/2}, \quad \eta = \left(\frac{\nu^3}{\langle \epsilon \rangle} \right)^{1/4}, \quad (3.1a,b)$$

where ϵ is the viscous dissipation rate and r represents the radial direction. Hence, the Reynolds number based on the Taylor microscale Re_λ can be defined as

$$Re_\lambda = \frac{\langle \rho \rangle \, \lambda_r \left[\langle u_r^2 \rangle \right]^{1/2}}{\mu}. \quad (3.2)$$

Dimotakis (2000) proposed that fully developed turbulent flow requires a Taylor Reynolds number $Re_\lambda \geq 100\text{--}140$. However, the critical Reynolds number is sufficient but not necessary (Robey *et al.* 2003). The temporal scales for turbulent cascade are not negligible, especially for the formation of the inertial subranges. The minimum state proposed by Zhou (2007) requires the Taylor Reynolds number $Re_\lambda \geq 560$. In our numerical simulations we calculate the Taylor microscale within the mixing region over time and show the Taylor Reynolds number Re_λ in figure 3. After reshock, the Taylor Reynolds number Re_λ gradually increases in the early period, which corresponds to the transition to turbulent mixing. Then, the Taylor Reynolds number Re_λ gradually decreases because of the apparent role of viscosity. The time diagrams of the two cases are similar, and their maximums satisfy the requirements of the critical Taylor Reynolds number. We also compute the Kolmogorov viscous scale at different radii and show the ratio of the grid scale and Kolmogorov viscous scale at two instants in figure 3. According to the criteria of DNS (Pope 2010), the grid resolution is enough to capture the vast majority of scales.

In contrast to the case without a chemical reaction, the Reynolds number of the case with a chemical reaction is smaller, and the Kolmogorov viscous scale is larger. This phenomenon means that turbulent flows with chemical reactions are less developed, and the main reason is the heat release effect of the chemical reaction.
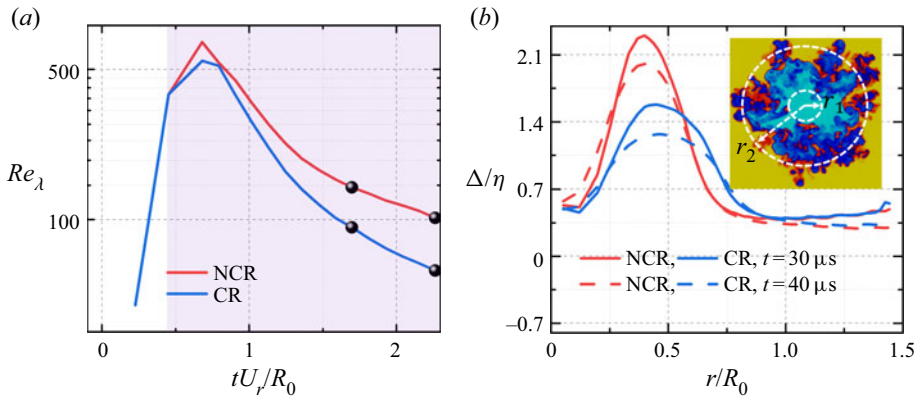
Figure 3. (*a*) Taylor Reynolds number Re_λ over time, where the black spheres correspond to the times of (*b*). The lilac area corresponds to the status after reshock. (*b*) The ratio of grid scale and Kolmogorov viscous scale over radius at two different times. The inset shows the contour slice of mixture density on the *x–y* slice at $t = 40\,\mu s$ without a chemical reaction, which illustrates inner and outer radii of the mixing region. Here NCR indicates a non-chemical reaction, and CR indicates a chemical reaction.

3.3. *Mixing width*

Most studies have dealt with the mixing of two fluids, and the mixing width has always been defined as the regions of mass fraction with threshold 1 %–99 % (or 5 %–95 %) (Mikaelian 2005; Zhou 2017*a*; Mikaelian & Olson 2020). The classic definition of mixing width cannot be successfully applied to our numerical simulations involving more fluids or elements, but we indeed need a specific definition of mixing width for a chemical reaction. From the element diffusion point of view, hydrogen diffuses out from the inside, and oxygen diffuses from the outside. According to this physical process, we propose the following two definitions of mixing width.

The first definition deals with species involving only hydrogen and oxygen with a threshold of 5 %. More precisely, the total fraction of species H and species H2 with threshold 5 % is employed to define the outer radius r_2, and the total fraction of species O and species O2 with threshold 5 % are employed to define the inner radius r_1. Hence, the mixing width can be obtained by the difference between the outer and inner radii.

In contrast, the second definition deals with species involving all hydrogen and oxygen with a threshold of 5 %. Rather, the total fraction of hydrogen from species H, species H2, species OH, species H2O, species H2O2 and species HO2 with threshold 5 % is used to define the outer radius r_1. The total fraction of oxygen from species O, species O2, species OH, species H2O, species H2O2 and species HO2 with a threshold of 5 % is used to define the inner radius r_2. The mixing width is the difference between the outer and inner radii. The above two definitions are the same for the case without a chemical reaction. Of course, 1 % can also be selected as the threshold, and negligible differences in statistical results exist in our numerical simulations (Ramaprabhu *et al.* 2012).

Based on the above two definitions, we compute the inner radius r_1 and outer radius r_2 of mixing regions with and without chemical reactions in figure 4(*a*,*c*). The inner radii based on the two definitions are nearly the same with and without chemical reactions, and the difference lies in the outer radius. The outer radius without a chemical reaction approaches a constant in the late stage. However, with a chemical reaction, the outer radius increases gradually over time, and the growth rate of the outer radius based on the second definition is larger than that based on the first definition. The principal reason is that the chemical reaction in our simulation is non-premixed, and the chemical reaction mainly
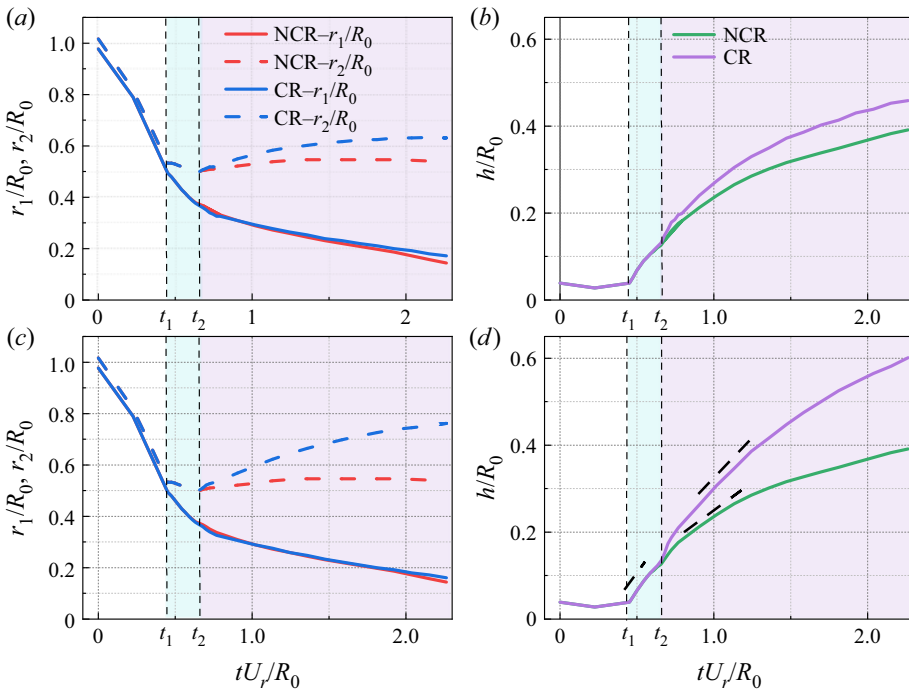
Figure 4. (*a*) The inner radius r_1 and outer radius r_2 of mixing regions based on the first definition with and without chemical reactions over time. (*b*) The mixing widths based on the first definition with and without chemical reactions over time. (*c*) The inner radius r_1 and outer radius r_2 of mixing regions based on the second definition with and without chemical reactions over time. (*d*) The mixing widths based on the second definition with and without chemical reactions over time. The black dashed lines mark the stages of the linear growth.

occurs around the outer radius. The mixing widths obtained from the corresponding outer and inner radii with and without chemical reactions are shown in figure 4(*b*) (based on the first definition) and (*d*) (based on the second definition). Similar to the regularities of the outer radius, the growth rate of the mixing width with a chemical reaction is larger than that without a chemical reaction. The discrepancy becomes apparent from the moment of reshock, which indicates the occurrence of the chemical reaction because of sufficient mixing of reactants.

We select the isosurfaces of the hydrogen fraction of the first and second definitions at two typical instants to show the discrepancy of the above two definitions in figure 5. Chemical reactions mainly occur around the outer radius, and small-scale structures with more sufficient mixing are easily dissipated. Hence, large-scale bubbles around the outer radius are dominant with a chemical reaction. Comparing the isosurfaces in figure 5(*a–c*), we find that the second definition is superior for exhibiting large-scale bubbles. The isosurface in figure 5(*b*) shows that the first definition misses some diffusion information of some species and leads to incorrect spatial distributions and mixing width. The similar large- and small-scale structures without a chemical reaction and with a chemical reaction based on the first definition in figure 5 confirm this conclusion. At other instants, the regulations and discrepancies of their spatial distributions are similar, and the numerical results at $t = 26\,\mu s$ in the late stage also illustrate that the second definition is suitable for the mixing width with multiple species mixing. Hence, we select the second definition to define the mixing width in later sections.
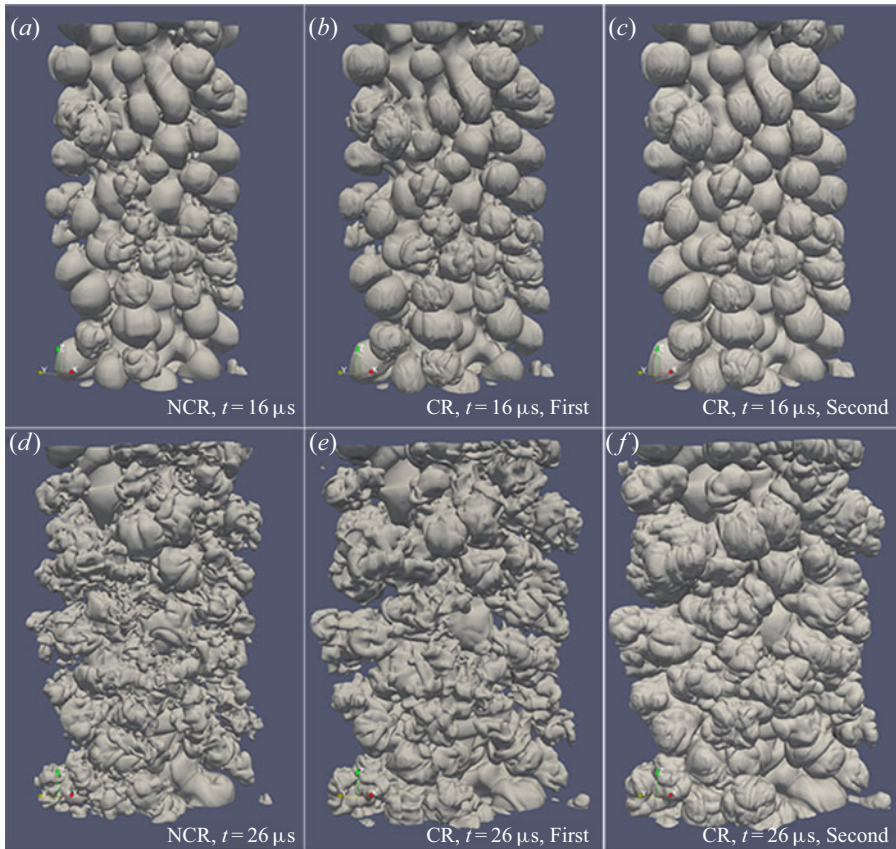
Figure 5. The three-dimensional isosurfaces of hydrogen corresponding to the first definition of the mixing width at $t = 16\,\mu s$ without a chemical reaction (*a*) and with a chemical reaction (*b*), and at $t = 26\,\mu s$ without a chemical reaction (*d*) and with a chemical reaction (*e*). The three-dimensional isosurfaces of all hydrogen elements including species H, species H2, species OH, species H2O, species H2O2 and species HO2, corresponding to the second definition of the mixing width with a chemical reaction at $t = 16\,\mu s$ (*c*) and at $t = 26\,\mu s$ (*f*).

In RMI with cylinder geometry, a simple prediction model with an incompressible equation that captures the convergence effect (Mikaelian 2005) is

$$h = cA\triangle vtR_0/R, \tag{3.3}$$

where c is a constant, A is the Atwood number, $\triangle v$ is the velocity difference before and after the shock wave and R is the cylinder radius. This model has been validated in cylindrical convergent RMI with two fluids (Mikaelian 2005; Lombardini & Pullin 2009). This linear model is also validated in the present numerical simulations with and without chemical reactions in figure 4(*d*), except around the instants of the first and second reshock. From the instant of the interaction of the reshock and the inner radius of the mixing regions, the mixing regions are compressed, and then stretched after the interaction of the reshock and the outer radius. The linear growth of the mixing regions is destroyed by the compressing and stretching effects. These effects are more apparent, especially around the second reshock than the first reshock, and the main reason may come from the wider mixing regions. Subsequently, the growth of the mixing width would be linear. After a full development with sufficient time, the growth of the mixing width might be self-similar.
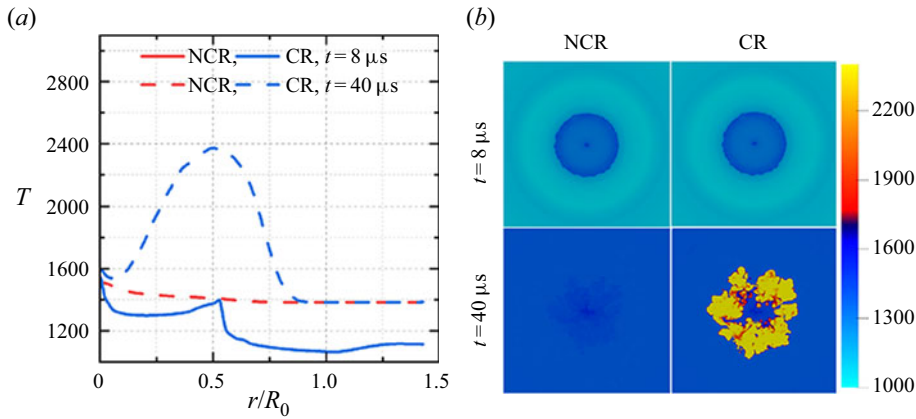
941 A55-12

Figure 6. (*a*) Temperature profiles over radius with and without chemical reactions at different times, and the temperature profiles with and without chemical reactions overlap at $t = 8\,\mu\text{s}$. (*b*) Contour slices of the temperature distribution on the *x*–*y* slice, corresponding to the status in (*a*).

There may exist many possible reasons for the quicker growth of the mixing width with a chemical reaction. First, a large number of products are present around the outer radius, and the Atwood number is changed dramatically. The Atwood number effect may be one of the prime causes. Although Dimonte & Schneider (2000) provided the Atwood number dependence, we could not obtain a specific Atwood number dependence for the growth rate of mixing widths because of various Atwood numbers in the process of a chemical reaction. Second, the combustion waves would be produced within the mixing regions, and propagate inwardly and outwardly. The heat release of chemical reactions leads to a large temperature difference, which is suitable for mixing. To confirm this explanation, we show the temperature profiles over radius at the instant of reshock and the late time in figure 6(*a*) and contour slices of the temperature distribution with and without chemical reactions in figure 6(*b*). After reshock, the mixing is not sufficient for a chemical reaction, and the temperature profiles with and without chemical reactions overlap at $t = 8\,\mu\text{s}$. In the late stage, the temperature increases dramatically along with heat release, especially in the mixing regions. However, the temperature rise without a chemical reaction is smaller.

3.4. *Chemical reaction description*

This section highlights the statistical characteristics of the chemical reaction, including the internal energy, heat release and consumption and production rates. In the early stage, it needs to absorb energy from flow fields to promote the development of the chemical reaction. Subsequently, it releases heat into flow fields to increase the temperature. However, the propagation of shock waves also leads to an increase in internal energy. Hence, we investigate these statistical characteristics individually.

As a part of total energy, the internal energy is extracted from (2.2) as

$$Ei = \sum_{m=1}^{N} \rho_m h_m - p. \tag{3.4}$$

We show the mean internal energy within the mixing regions with and without chemical reactions in figure 7. There exists an apparent discrepancy of the internal energy with and without chemical reactions, especially in the late stage. The mean internal energy with a
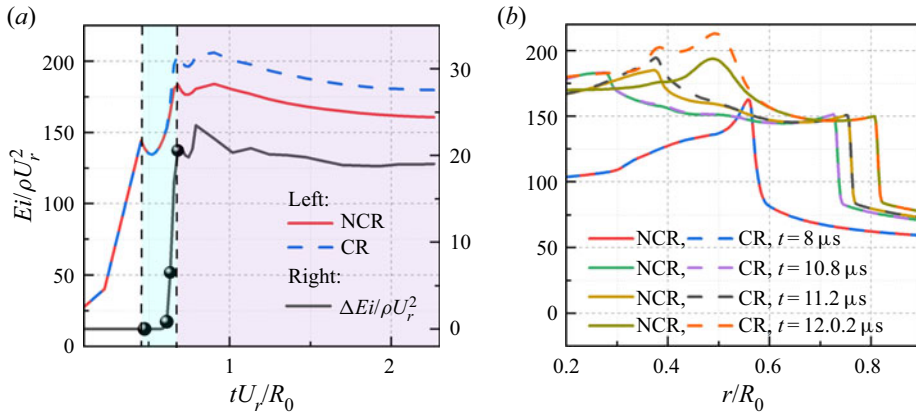
Figure 7. (*a*) The mean internal energy with and without chemical reactions over time, and their difference is shown on the right vertical axis. (*b*) The internal energy with and without chemical reactions over radius at four different times corresponding to (*a*).

chemical reaction is larger due to the heat release effect. With the development of mixing width, the mean internal energies within the mixing regions with and without chemical reactions decrease. The decay of the mean internal energy in figure 7(*a*) originates from the increase of the mixing regions. The chemical reaction would be weakened with the decrease of the fuels around the mixing centre in the late time. Non-reactive oxygen is rolled up into the mixing regions, and is transported towards the mixing centre. With the development of the mixing regions, more time is needed for the oxygen transportation to reach a fully mixed status. The discrepancy can not be negligible after the first reshock, and becomes apparent subsequently. The radial distribution in figure 7(*b*) indicates that the increased internal energy induced by a chemical reaction is smaller than that by shock propagation in the current situation. We infer that if the Mach number is larger, the internal energy change induced by shock propagation would be more dominant.

The internal energy change cannot be directly associated with the chemical reaction because the presence of viscosity also transfers energy from kinetic energy into internal energy. The heat released by a chemical reaction is explored directly in figure 8. The heat release only originates from the chemical reaction, and we focus on its temporal evolution and radial distributions of the case with a chemical reaction. Consistent with the internal energy change, the mean heat release comes from a negative value in the early stage to a positive value after the first reshock. The rapid development of the mean heat release after the first reshock is consistent with transition and turbulent mixing development. Both the subsequent decay of the mean heat release in figure 8(*a*) and the lower values around the outer radius in figure 8(*b*) come from the development of the mixing regions. The radial distribution of the mean heat release after the first reshock in figure 8(*b*) reveals that the chemical reaction releases heat into flow fields, and the mean heat release increases rapidly in the subsequent times.

In order to evaluate the spatial distribution of heat release, we show the contour slices of heat release at the plane of $z = L_z/2$ at different instants in figure 9. In the early stage of figure 9(*a*) the value of the heat release is negative, and it means that the chemical reaction absorbs energy from the flow fields. After the first reshock (figure 9*b*), the value of the heat release is positive, which indicates the beginning of the chemical reaction effect. With the development of transition and turbulent mixing, the heat release increases dramatically.
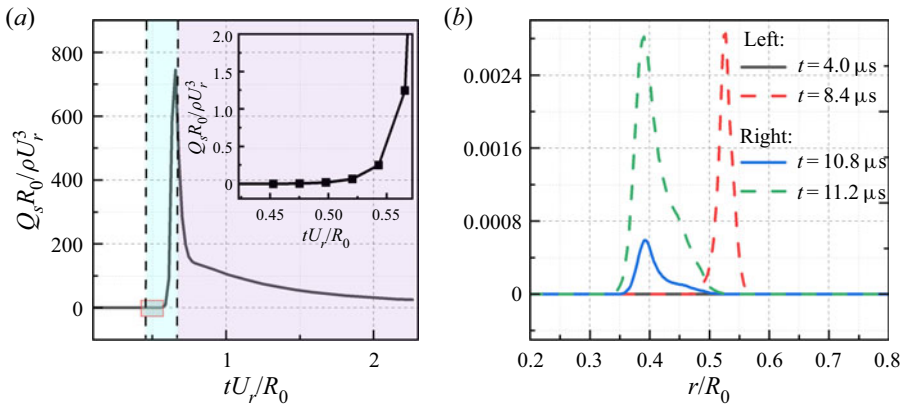
Figure 8. (*a*) The mean heat release over time, and the inset shows its temporal evolution after the first reshock. (*b*) The mean heat release over radius at four different times.
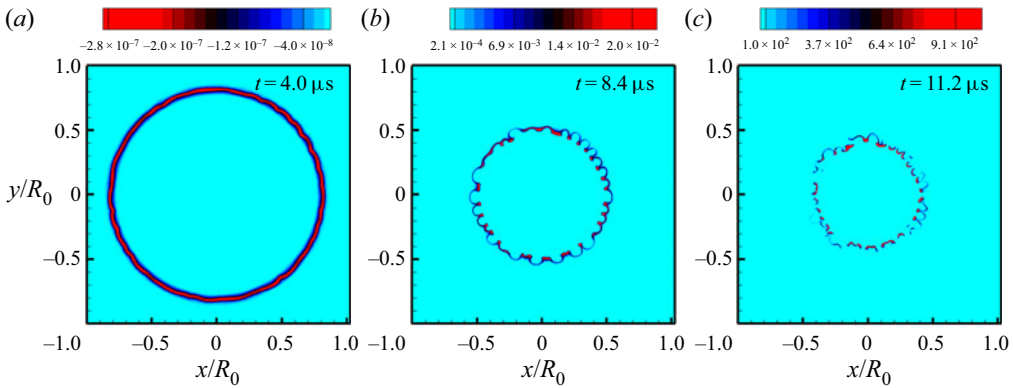

Figure 9. Contour slices of the heat release at three different instants.

Due to the initial non-premixed configuration, the chemical reaction only appears within the mixing regions.

The consumption of hydrogen and oxygen and water production can be regarded as a direct measurement of the chemical reaction. We exhibit the mean consumption and production rates in figure 10. Consistent with the trend of heat release, the chemical reaction is apparent before the second reshock. The subsequent decay originates from the decay of turbulent fluctuations and the development of mixing regions. The radial distributions of reactants and products at different instants in figure 10(*b*) also reveal that the consumption of reactants and the production of products begin to be apparent after the first reshock.

The contour slices of the consumption and production rates at three different instants are exhibited in figure 11. For the same instant, the contour slices of the consumption and production rates are similar, and we just show one of them at different instants for the sake of simplicity. The heat release is associated with the consumption and production rates, and their spatial distributions before and around the instant of the first reshock in figure 11(*a*,*b*) are similar to the results in figure 9. However, their spatial distributions are different around the instant of the second reshock with a high degree of turbulent mixing.
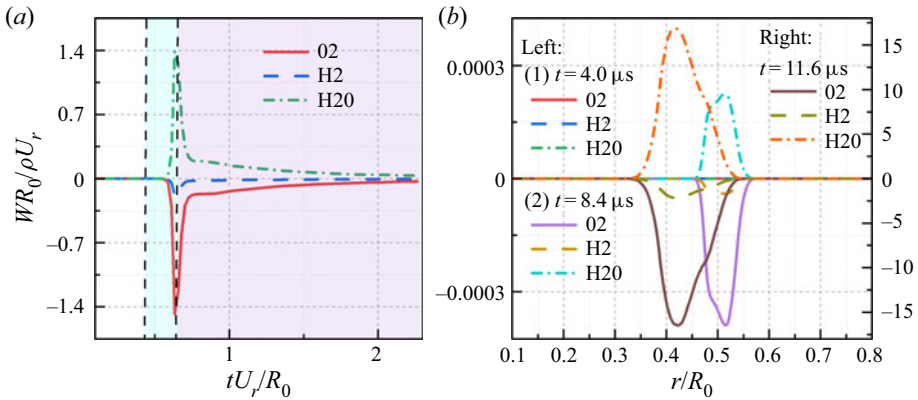
Figure 10. (*a*) The mean consumption and production rates over time. (*b*) The mean heat release over radius at three different times.
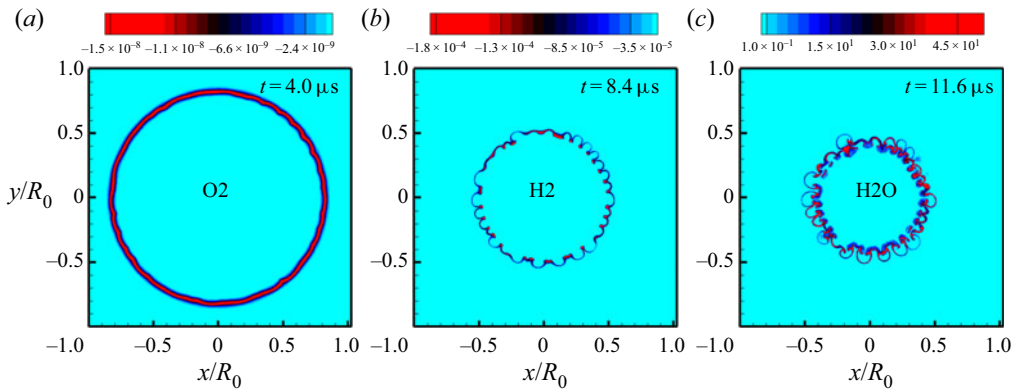

Figure 11. Contour slices of the consumption rate of oxygen (*a*) at $t = 4.0\,\mu s$, the consumption rate of hydrogen (*b*) at $t = 8.4\,\mu s$ and the production rate of water (*c*) at $t = 11.6\,\mu s$.

According to the definition of heat release, the discrepancy originates from the spatial discrepancy of temperature fields.

3.5. *Turbulent statistics*

In this section we carry out turbulent statistics of RMI with and without chemical reactions, especially focusing on the temporal evolution after reshock. The chemical reaction effects are reflected by some characteristic parameters, such as turbulent kinetic energy, enstrophy, helicity, viscous dissipation rate, palinstrophy, skewness, flatness, spectra and inter-scale fluxes.

3.5.1. *Turbulent kinetic energy*

To include the variable-density effects, the Favre-averaged technique is used to obtain the mean field as (Gatski & Bonnet 2013)

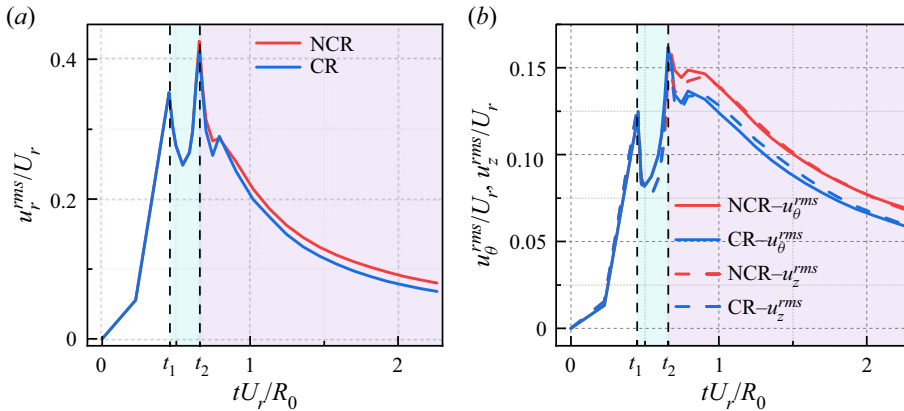$$\tilde{u}_i = \frac{\overline{\rho u_i}}{\bar{\rho}}, \tag{3.5}$$

Figure 12. (*a*) The r.m.s. of radial velocity with and without chemical reactions over time. (*b*) The r.m.s. of axial and circumferential velocity with and without chemical reactions over time.

where $\bar{\ }$ denotes the spatial average within mixing regions, and the fluctuating component is defined as $u_i'' = u_i - \tilde{u}_i$. In figure 12 we show the root mean square (r.m.s.) of radial, axial and circumferential velocity with and without chemical reactions over time to present the temporal developments of the anisotropy of the velocity field under the influence of a chemical reaction. The radial direction is dominant because of shock propagation. After reshock, the fluctuating development rate of radial velocity is smaller with a chemical reaction than that without a chemical reaction. In the late stage, the decay rates of all velocity components with a chemical reaction are faster because of larger viscous dissipation with heat release. The axial and circumferential directions are homogeneous, and their differences without a chemical reaction in figure 12(*b*) are negligible, especially in the late time. However, the differences of axial and circumferential components with a chemical reaction are apparent. This indicates that a chemical reaction hinders the anisotropy recovery process, which is different from classic decaying homogeneous and isotropic turbulence.

The turbulent kinetic energy is defined as

$$TKE = \frac{1}{2}\overline{\rho u''^2}. \tag{3.6}$$

According to the theoretical prediction of decaying homogeneous and isotropic turbulence, there exists a power-law solution of turbulent kinetic energy as $TKE \sim t^{-\theta}$ (Samtaney, Pullin & Kosović 2001). The value $\theta = 1$, based on the Kármán–Howarth similarity theory (Kármán & Howarth 1938). There are also other predictions, such as $\theta = 10/7$ based on the constancy of the Loitsianskii invariant, $\theta = 6/5$ based on assuming a constant Saffman invariant (Saffman 1967), and $\theta = 3/2$ based on the two-point longitudinal velocity correlation (Huang & Leonard 1994). Although Reynolds number dependence exists, the decay rates in RMI are always faster than those in classic homogeneous and isotropic turbulence (Groom & Thornber 2019, 2021). We computed the turbulent kinetic energy within the mixing regions and showed them in figure 13. We fitted the two numerical results in figure 13 and obtained the decaying exponent $\theta = 2.05$ without a chemical reaction and $\theta = 2.50$ with a chemical reaction. These two decay exponents are relatively large, which may originate from the relatively low Reynolds number in the present numerical simulations. Under the influence of chemical reactions, the decay rate
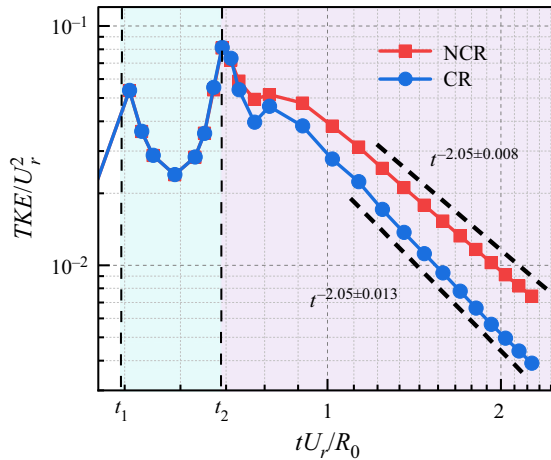
Figure 13. The turbulent kinetic energy with and without chemical reactions over time.

of turbulent kinetic energy is larger, which is also attributed to larger viscous dissipation with chemical reactions.

3.5.2. *Mixed mass*

The mixed mass can be regarded as a direct marker of the mixing regions, which is very important for experimental measurements (Zhou, Cabot & Thornber 2016; Zhang *et al.* 2020; Zhou *et al.* 2020; Bender *et al.* 2021). Because of the appearance of nitrogen, we need to deal with the case of three-species mixing. Hence, we extend the definition of the mixed mass for two-species diffusion to the case of three-species diffusion as

$$\Phi = \int 27\rho Y_1 Y_2 Y_3 \, \mathrm{d}V, \tag{3.7}$$

where Y_1, Y_2 and Y_3 are the mass fractions, and $Y_1 + Y_2 + Y_3 = 1$. The coefficient 27 is introduced to assure that the mixed mass is $\int \rho \mathrm{d}V$ if the three mass fractions are equal, and it is similar to the consideration of the coefficient for the two-species diffusion (Zhang *et al.* 2020). After a simple deduction based on the mass equation (2.1*a*) and species equation (2.1*d*), we can obtain the governing equation of the mixed mass as

$$\frac{\mathrm{d}}{\mathrm{d}t} \int 27\rho Y_1 Y_2 Y_3 \, \mathrm{d}V = 27 \int \rho D_m \frac{\partial Y_m}{\partial x_j} \frac{\partial (Y_n Y_l)}{\partial x_j} \, \mathrm{d}V, \quad (m, n, l = 1, 2, 3, \, m \neq n \neq l). \tag{3.8}$$

The above governing equation indicates that the newly defined mixed mass is also a conserved quantity, and its temporal evolution originates from the diffusion process. In order to evaluate the mixed mass at the initial time, we adopt the hyperbolic tangent function present in (2.12) to determine the mass fraction distributions. The hydrogen is placed inside the perturbed interface for the current configurations, and the oxygen is placed outside the perturbed interface. The nitrogen distributes inside and outside the perturbed interface with different volume fractions. The species distributions along the radial direction are shown schematically in figure 14. We assume that the density involved in the definition of the mixed mass does not affect the boundedness, and we focus on the
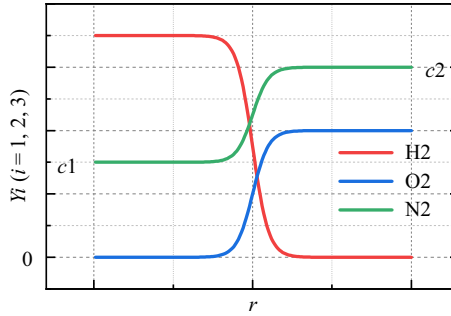
Figure 14. The schematic configuration of the three-species distributions with hyperbolic tangent function. The $c1$ and $c2$ denote the mass fractions of nitrogen inside and outside the perturbed interface, respectively.

remaining part. The distributions of mass fractions are expressed as

$$Y_1 = \frac{1 - c2}{2}\left[1 + \tanh(r)\right], \; Y_2 = \frac{c2 - c1}{2}\left[1 + \tanh(r)\right] + c1, \; Y_3 = 1 - Y_1 - Y_2, \quad (3.9)$$

where $c1$ denotes the mass fraction of nitrogen within the perturbed interface and $c2$ denotes the mass fraction of nitrogen without the perturbed interface. The remaining part can be computed as

$$\int_{-\infty}^{+\infty} Y_1 Y_2 Y_3 \, \mathrm{d}r = \frac{(c1 + c2)(1 - c1)(1 - c2)}{4}. \quad (3.10)$$

The boundedness of the mixed mass in the initial time indicates that the expression (3.7) might be appropriate. In addition, the boundedness of the expression (3.7) can also be proven through the error function distribution of the involved species.

Correspondingly, the normalized mixed mass can be defined as

$$\Psi = \frac{\int \rho Y_1 Y_2 Y_3 \, \mathrm{d}V}{\int \bar{\rho}\bar{Y}_1 \bar{Y}_2 \bar{Y}_3 \, \mathrm{d}V}. \quad (3.11)$$

The normalized mixed mass measures the mixing degree within the mixing regions, and it corresponds to 1 for the completely mixed fluid and 0 for the complete segregation, respectively. Here, the subscript $1, 2$ and 3 may correspond to oxygen, nitrogen and hydrogen, respectively.

The differences of the mixed masses and normalized mixed masses with and without chemical reactions are shown in figure 15, and the mixed masses and normalized mixed masses with and without chemical reactions are shown in the inset of figure 15. We select the initial mass within the perturbed interface to normalize the mixed mass. The mixed masses with and without chemical reactions are approximately up to 2 % of the initial mass within the perturbed interface, and the difference of the mixed masses is approximately up to 0.2 %. The tendency of the normalized mixed mass is consistent with the results of classical mixed mass for two-species diffusion (Zhou *et al.* 2016), and the asymptotic value is approximately 0.6. The slight difference with the results in Zhou *et al.* (2016) might originate from the effects of shock strength, Atwood number, convergence, etc. Both the mixed mass and normalized mixed mass results indicate that the chemical reaction leads to a weak mixing, although it leads to faster growth of the mixing width. The weak mixing also originates from the heat release effect of the chemical reaction.
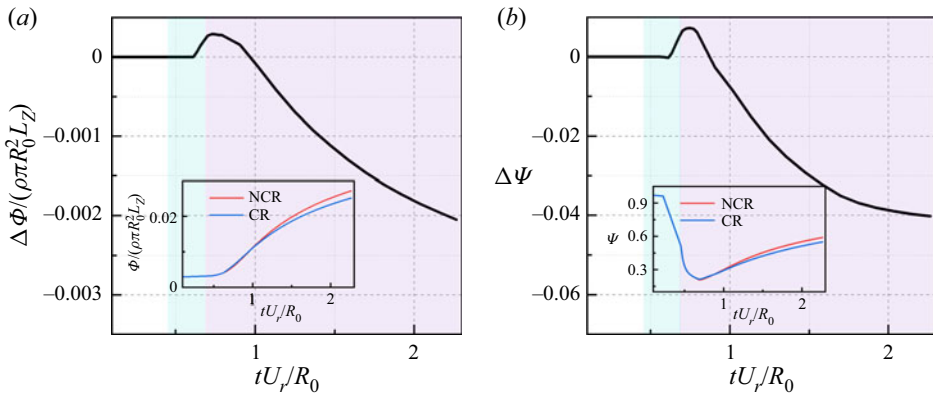
Figure 15. (*a*) The difference of the mixed masses with and without chemical reactions over time. The inset shows the mixed masses with and without chemical reactions over time. (*b*) The difference of the normalized mixed masses with and without chemical reactions over time. The inset shows the normalized mixed masses with and without chemical reactions over time.

3.5.3. *Enstrophy and helicity*

The enstrophy and helicity within the mixing regions are defined as

$$\Omega_{tot} = \int_V \overline{\left(\frac{\omega_i\omega_i}{\rho}\right)}\,dV, \quad H = \overline{u_i\omega_i}. \tag{3.12}$$

The enstrophy is used to feature the strength of vorticity, and the helicity reflects the broken degree of symmetry (Moffatt & Tsinober 1992; Yan *et al.* 2020*b*). We show them with and without chemical reactions over time in figure 16. For enstrophy, chemical reactions hinder its development after reshock, and the decay rate is also larger than that without chemical reactions. Later, we fit the two numerical results and obtained decay rate $\theta = 1.66$ without a chemical reaction and $\theta = 1.98$ with a chemical reaction, which are larger than the numerical consequence in planar geometry with $\theta = 1.4$ (Zhou *et al.* 2020). The discrepancy originates from the low-Reynolds-number effect in the present numerical simulations. The numerical results in figure 16(*b*) indicate the development of helicity, especially after reshock, along with turbulence development, and it might be marked as the transition or development of turbulence. In RMI with cylindrical geometry, the flows develop from quasi-two dimensions into three dimensions. The mathematical property of helicity can capture the transition process. In the late stage the changes of helicity are not monotonous, which might be attributed to chirality transfer along with viscous dissipation (Yan *et al.* 2020*a*). Because of chemical reactions, the helicity developments after reshock are hindered, and they correspond to weaker fluctuations.

The radial distributions of enstrophy and helicity within the mixing regions at two characteristic instants marked in figure 16 are shown in figure 17. The first instant at $t = 12\,\mu s$ corresponds to the later development of perturbed interfaces compressed by reshock, and the second instant $t = 13.2\,\mu s$ corresponds to the developed peak of the perturbed interfaces after reshock. With time passing, the developed enstrophy is mainly reflected as outer layers of mixing regions. The possible reason is that multiple reflected shock waves propagate between the centre and mixing regions, and the enstrophy is strengthened through baroclinic vorticity induced by multiple shock waves. The chemical reaction mainly occurs around the outer radius because of the full mixing of fuel and oxygen. The combustion wave propagates towards both the centre and outer regions, and
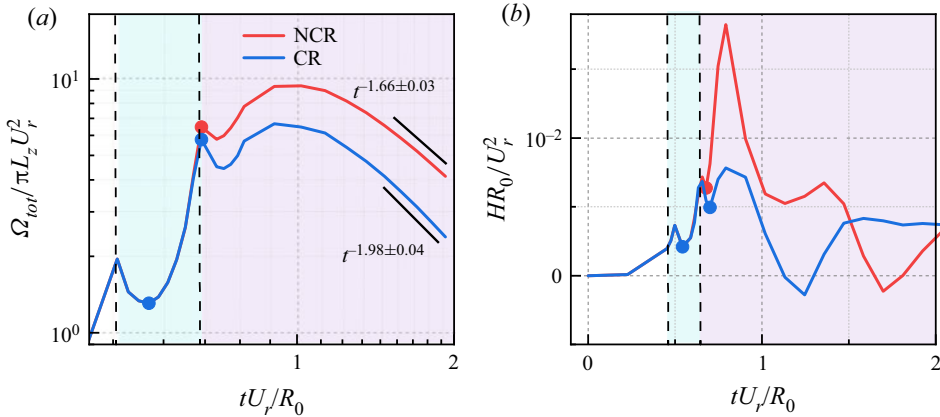
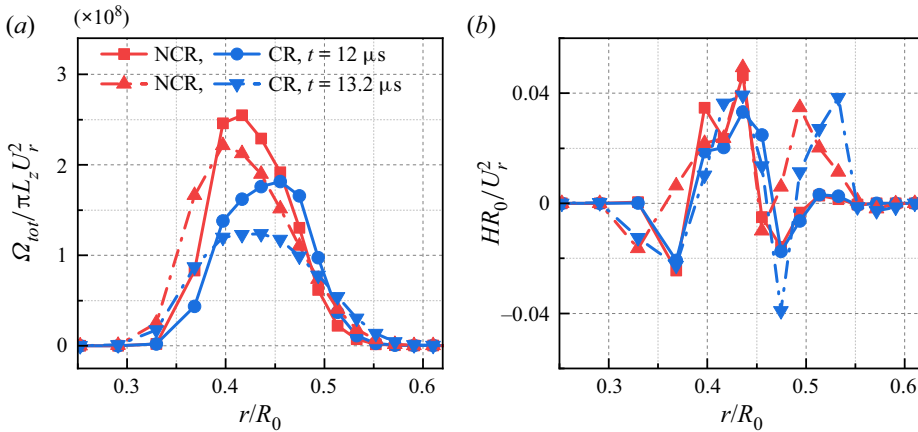Figure 16. Enstrophy (*a*) and helicity (*b*) with and without chemical reactions over time.

Figure 17. Distribution of enstrophy (*a*) and helicity (*b*) with and without chemical reactions along the radial direction at $t = 12\,\mu\text{s}$ and $t = 13.2\,\mu\text{s}$.

the combustion wave represented as a high-pressure gradient leads to a higher baroclinic vorticity (Attal & Ramaprabhu 2015), which promotes the development of enstrophy in the outer layers of the mixing regions. For helicity along with radial distribution, the multiple shock wave and combustion wave effects are similar to those of enstrophy, especially around the outer layers of mixing with a chemical reaction. The radial distribution of helicity might not be regular in contrast to enstrophy, which reflects the complexity of helicity, and this will be further explored in the future.

3.5.4. *Palinstrophy*

To explore the viscous dissipation mechanism of enstrophy, we derive the averaged governing equations of enstrophy in compressible flows as

$$\frac{\mathrm{d}}{\mathrm{d}t}\overline{(\omega_i\omega_i)} = \overline{\omega_i\omega_j\frac{\partial u_i}{\partial x_j}} - \overline{2\omega_i\omega_i\frac{\partial u_k}{\partial x_k}} + \overline{\frac{2}{\rho^2}\varepsilon_{ijk}\omega_i\frac{\partial\rho}{\partial x_j}\frac{\partial p}{\partial x_k}} + \overline{2\varepsilon_{ijk}\omega_i\frac{\partial}{\partial x_j}\left(\frac{1}{\rho}\frac{\partial\sigma_{lk}}{\partial x_l}\right)}. \quad (3.13)$$
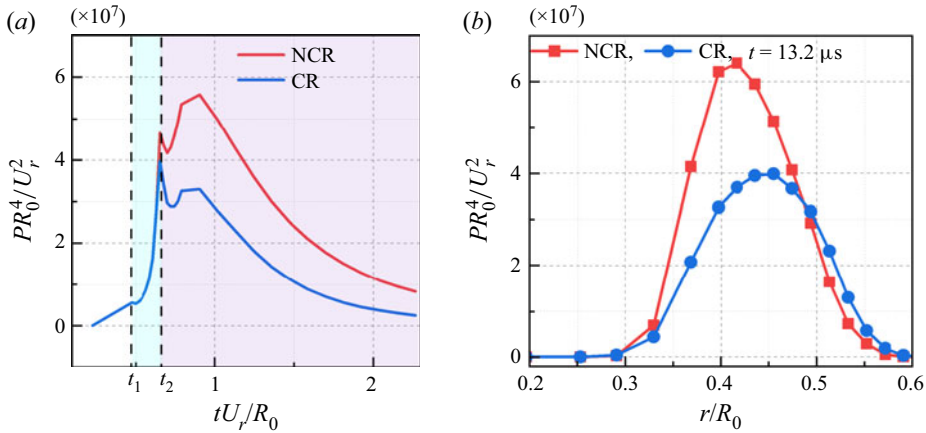
Figure 18. (*a*) Palinstrophy with and without chemical reactions over time. (*b*) The distribution of palinstrophy along the radial direction at $t = 13.2\,\mu s$.

In the incompressible limit the viscous term can be rewritten as $-2\nu P(t)$, and $P(t)$ is the palinstrophy defined as

$$P(t) = \frac{1}{2}\overline{(\nabla \times \omega)^2} = \int_0^{+\infty} k^4 E(k, t)\, dk, \qquad (3.14)$$

where $k = |\boldsymbol{k}|$, $\boldsymbol{k}$ is the wavenumber and $E(k, t)$ is the energy spectrum density (Lesieur 1997). The palinstrophy highlights the small-scale structures and the tightening of vorticity contours (Gauthier 2017), and it is related to the skewness factor for isotropic turbulence (Batchelor & Townsend 1947). In two-dimensional turbulent flows the palinstrophy increases with enstrophy cascading to larger wavenumbers (Pouquet *et al.* 1975; Tran & Dritschel 2006).

In compressible flows, if we assume the kinematic viscosity coefficient is a constant, the viscous term of (3.13) is the same as that in incompressible flows. This means that the viscous dissipation of enstrophy in three-dimensional compressible flows does not concern compressibility, and the theoretical achievements in incompressible flows also apply to compressible flows.

In figure 18 we show the palinstrophy averaged within mixing regions over time and the radial distribution at $t = 13.2\,\mu s$. The development of palinstrophy is behind enstrophy and after reshock because different time scales exist for enstrophy and palinstrophy. The amplitude of the palinstrophy with a chemical reaction is smaller than that without a chemical reaction, and it originates from a higher viscosity coefficient of the heat release effect. The smaller the scales, the more apparent the role of viscosity. Hence, the palinstrophy reflecting small scales is damped by higher viscosity. The damping effect of a chemical reaction is also reflected on the radial distributions of palinstrophy in figure 18(*b*), especially on the inner and centre mixing regions. Around outer regions, the palinstrophy with a chemical reaction is slightly larger, which also results from the high-pressure gradient because of combustion waves. The outer mixing region with a chemical reaction is underdeveloped, and the baroclinic vorticity promotes small-scale developments.

941 A55-22

3.5.5. *Skewness and flatness*

For any random variable X, the skewness and flatness are defined as

$$S = \frac{\langle X^3 \rangle}{\langle X^2 \rangle^{3/2}}, \quad F = \frac{\langle X^4 \rangle}{\langle X^2 \rangle^2}. \tag{3.15a,b}$$

The skewness measures the asymmetry of probability distribution functions (p.d.f.s), and the flatness measures the discrepancy degree from a Gaussian distribution (Sahoo, Bonaccorso & Biferale 2015).

Orszag (1977) proposed that for decaying isotropic turbulent flows, the relation of skewness of velocity gradient and palinstrophy is

$$S(t) = 2.35 \frac{\nu P(t)}{(\omega_i \omega_i)^{3/2}}. \tag{3.16}$$

Although this identity relation is no longer valid in the present three-dimensional RMI with and without chemical reactions, it also reflects the relationship of skewness and palinstrophy, and both of them highlight the small scales.

In figure 19 we show the skewness and flatness of velocities in the radial and circumferential directions. The statistical results of velocity in the axial direction are similar to those in the circumferential direction, and we do not show them for the sake of simplicity. For the velocity skewness, the radial velocity skewness is larger than that in the circumferential or axial directions. Because the radial direction is dominant, it corresponds to a larger asymmetry of radial velocity. In the early stage after reshock, the skewness increases monotonically during the shock compression process on the perturbed interface and during the development process. When the skewness is large enough, the role of multiple weaker shock compressions is apparent. The damping effects of the chemical reaction are reflected in the smaller skewness of velocity. The flatness of the dominant radial velocity in figure 19(*b*) is smaller, which indicates that the higher-order moments affected by the main shock wave are not fully developed. In contrast, the higher-order moments of circumferential velocity can eliminate the constraint effects of radial direction mixing, and small scales can be developed more fully. In the late time the flatness with a chemical reaction is larger, and it corresponds to a more intermittent status. Hence, a larger flatness means a larger discrepancy from the Gaussian distribution, and a smaller skewness means a weaker asymmetry with the chemical reaction.

In addition, we compute the skewness and flatness of the mixture density and temperature with and without chemical reactions in figure 20. Before reshock, the discrepancies of skewness and flatness with and without chemical reactions are negligible. For the density field, a chemical reaction involves more element mixing, and the skewness and flatness are larger than those without a chemical reaction. For the temperature field, at the early stage after reshock, the skewness and flatness are larger because of heat release effects, especially around the outer layer of mixing regions. As time passes, the discrepancy degree of skewness with and without chemical reactions decreases. With fuller mixing of fuel and oxygen after reshock, the chemical reaction apparently begins to occur, and the combustion wave propagates towards two sides. At the early stage of a chemical reaction, the temperature varies dramatically, leading to larger skewness and flatness. The temperature gradient decreases with the propagation of combustion waves, and the skewness and flatness also decrease. In the late time the temperature field becomes smoother with higher viscosity and results in smaller skewness and flatness. The higher-order moment is more sensitive to the propagating combustion waves.
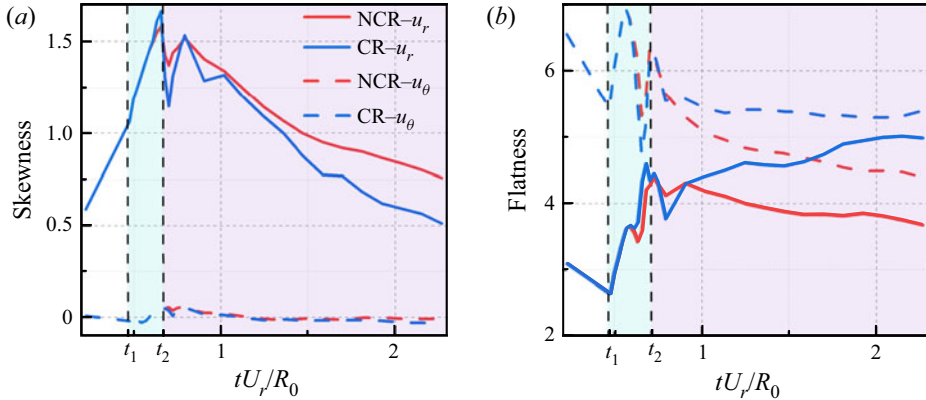
Figure 19. The skewness (*a*) and flatness (*b*) of radial u_r and circumferential u_θ velocity with and without chemical reactions over time.
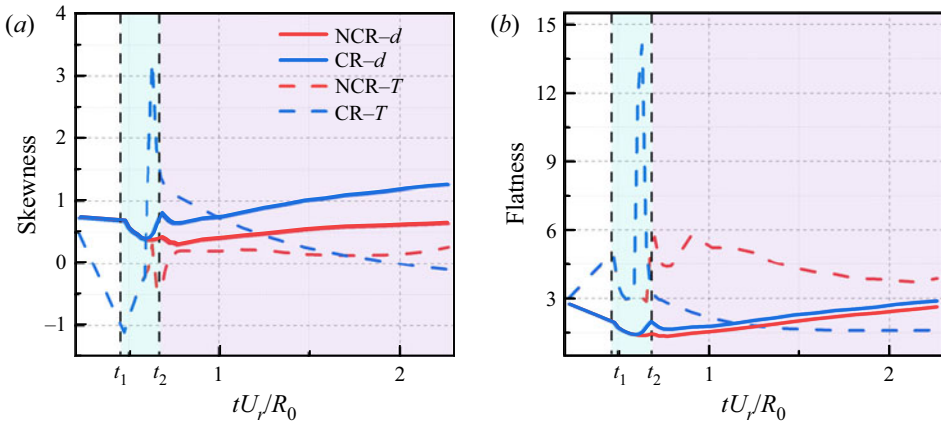

Figure 20. Skewness (*a*) and flatness (*b*) of mixture density and temperature with and without chemical reactions over time.

3.5.6. *Viscous dissipation rate*

The ensemble-averaged enstrophy is associated with viscous dissipation (Yeung, Zhai & Sreenivasan 2015), and we rewrite the ensemble-averaged enstrophy in compressible flows as

$$\left\langle \omega^2 \right\rangle = \frac{1}{2} \left\langle \left(\frac{\partial u_i}{\partial x_j} - \frac{\partial u_j}{\partial x_i} \right) \left(\frac{\partial u_i}{\partial x_j} - \frac{\partial u_j}{\partial x_i} \right) \right\rangle = \left\langle \frac{\partial u_i}{\partial x_j} \frac{\partial u_i}{\partial x_j} \right\rangle - \left\langle \frac{\partial u_i}{\partial x_j} \frac{\partial u_j}{\partial x_i} \right\rangle . \tag{3.17}$$

The ensemble-averaged viscous dissipation rate ϵ reads as

$$\epsilon = \left\langle \sigma_{ij} \frac{\partial u_i}{\partial x_j} \right\rangle = \left\langle \mu \left(\frac{\partial u_i}{\partial x_j} + \frac{\partial u_j}{\partial x_i} - \frac{2}{3} \theta \delta_{ij} \right) \cdot \frac{\partial u_i}{\partial x_j} \right\rangle . \tag{3.18}$$

Hence, if we assume the dynamic viscosity coefficient μ to be a constant in total flow fields, we can obtain the following relation:

$$\epsilon = \bar{\mu} \langle \omega^2 \rangle + \frac{4}{3} \bar{\mu} \langle \theta^2 \rangle + 2\bar{\mu} \left\langle \frac{\partial}{\partial x_k} \left[\frac{(u_k u_l)}{\partial x_l} - 2 u_k \theta \right] \right\rangle . \tag{3.19}$$
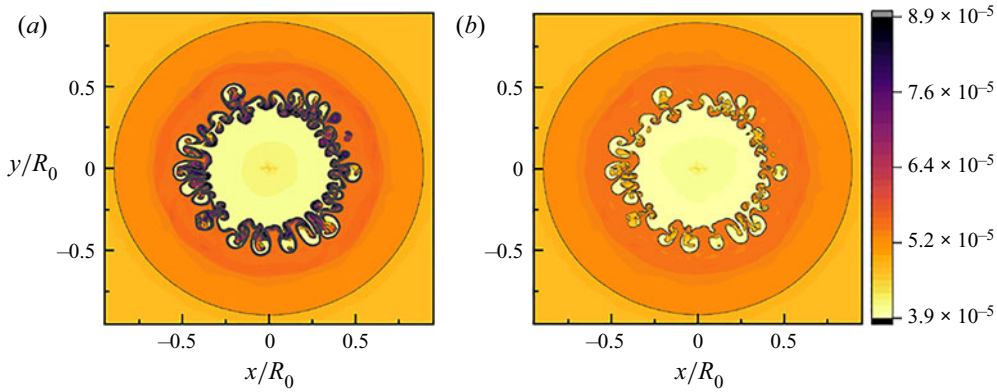
Figure 21. Two-dimensional contour slices of dynamic viscosity coefficient μ with a chemical reaction (*a*) and without a chemical reaction (*b*) at $t = 13.2\,\mu s$.

Here $\bar{\mu}$ is a mean dynamic viscosity coefficient defined by $\bar{\mu} = \langle \mu \rangle$, and the fluctuating dynamic viscosity coefficient is $\mu' = \mu - \bar{\mu}$.

However, the dynamic viscosity coefficient μ fluctuates dramatically along with the temperature field. We show contour slices of the dynamic viscosity coefficient μ with and without chemical reactions at $t = 13.2\,\mu s$ in figure 21. Compared with the case without a chemical reaction, the dynamic viscosity coefficient with a chemical reaction fluctuates more dramatically, especially around the mixing regions because of heat release effects. Hence, the averaged dynamic viscosity coefficient cannot be used to exactly predict the total viscous dissipation rate. The viscous dissipation rate with a chemical reaction should be investigated through coupling the dynamic viscosity coefficient, enstrophy and velocity divergence. This coupling effect highlights the discrepancy of viscous dissipation rates between incompressible and compressible turbulence, in addition to the pressure-work defect (Eyink & Drivas 2018).

The averaged viscous dissipation rate within the mixing regions with and without chemical reactions over time and their distributions along the radial direction are shown in figure 22. The evolution of viscous dissipation rates is consistent with turbulent kinetic energy under the influence of multiple shock compression. After reshock, the viscous dissipation rate decreases due to shock compression and develops after the shock propagates out from the mixing regions. The viscous dissipation rate decays self-similarly in the late stage. The decaying exponents obtained by fitting are 2.14 and 2.53 without a chemical reaction and with a chemical reaction, respectively. The viscous dissipation rates with chemical reactions are smaller than those without chemical reactions, even though the dynamic viscous coefficient with chemical reactions is larger. The main reason is that the velocity gradient with a chemical reaction is smaller, which is also reflected in the smaller enstrophy and palinstrophy. The radial distributions of the viscous dissipation rates in figure 22(*b*) reveal that the smaller velocity gradients mainly work around the mixing centre, and the larger dynamic viscosity coefficients mainly work around the outer layers with an apparent chemical reaction.

To visually investigate the spatial distributions of the viscous dissipation rates with and without chemical reactions, we show the three-dimensional surface diagrams of the viscous dissipation rates at some typical instants after reshock in figure 23. Because of the large velocity gradient across the shock, the viscous dissipation rates around the shock are dominant out of mixing regions. The spatial distributions of the viscous dissipation rates
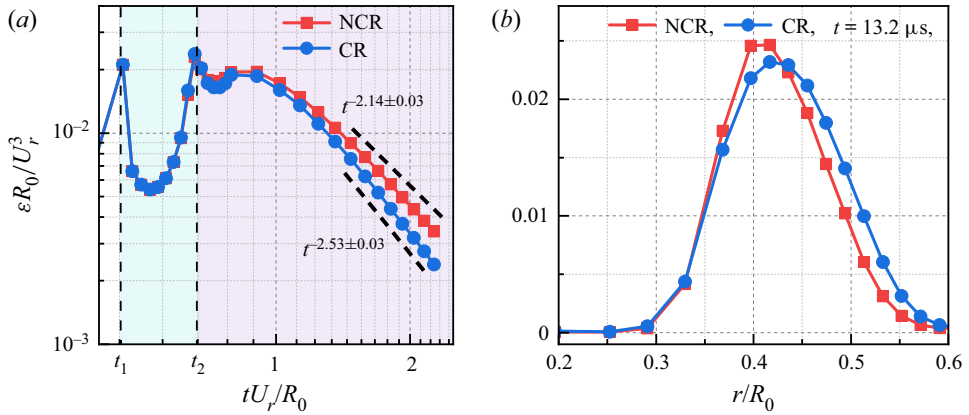
Figure 22. (*a*) Viscous dissipation rates with and without chemical reactions over time. (*b*) The distribution of viscous dissipations along the radial direction at $t = 13.2\,\mu s$.
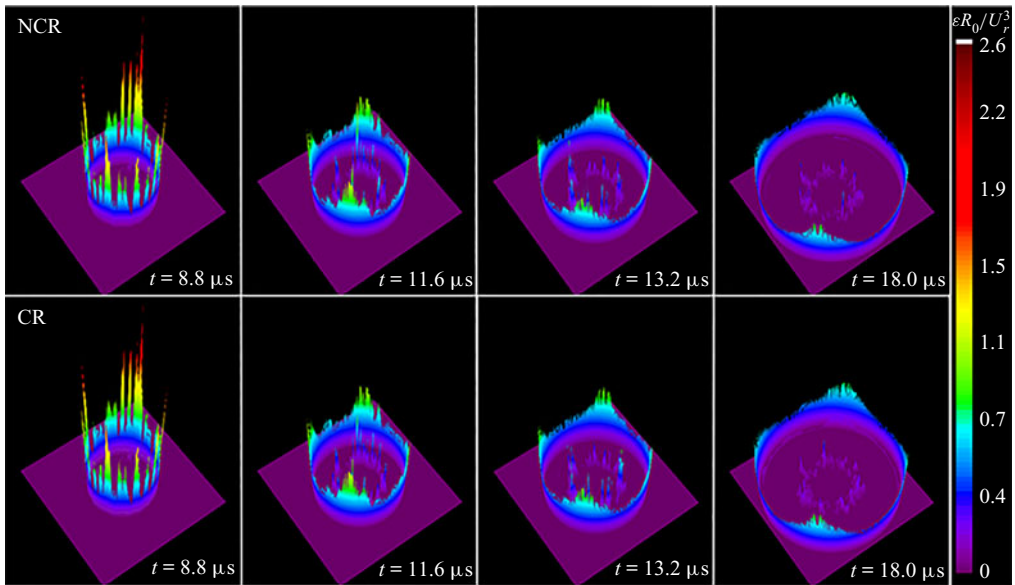

Figure 23. Three-dimensional surface diagrams of viscous dissipation rates with and without chemical reactions at some typical instants.

within the mixing regions are non-uniform, with many so-called extreme events (Yeung *et al.* 2015; Debue *et al.* 2021; Moffatt 2021). These local extreme viscous dissipation rates within the mixing regions are similar to fully developed turbulent flows, and they also decay with time. Compared with the case without a chemical reaction at the same instant, the mixing regions with a chemical reaction present more intermittent structures of viscous dissipation rates, and the discrepancies around the propagating shock are negligible.

The chemical reaction effects on the spatial distributions of the viscous dissipation rates are further explored by the p.d.f.s in figure 24. We select some typical instants at $t = 8.8\,\mu s$ with the early time of shock compression, at $t = 11.6\,\mu s$ with the late time of shock compression, and at $t = 13.2\,\mu s$ with development getting rid of shock compression.
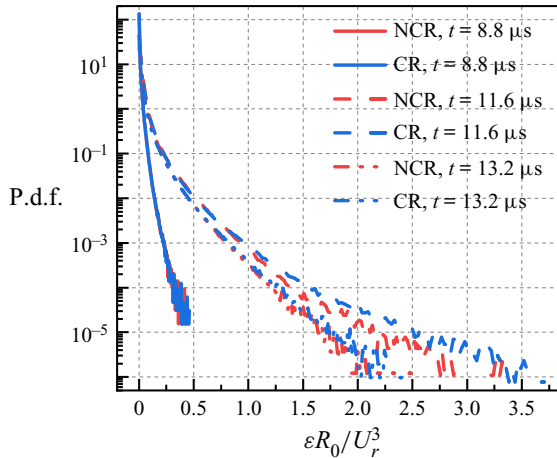
Figure 24. Probability distribution functions of the viscous dissipation rates with and without chemical reactions at $t = 8.8\,\mu s$, $t = 11.6\,\mu s$ and $t = 13.2\,\mu s$.

At $t = 8.8\,\mu s$, their discrepancies are negligible because the chemical reaction is not apparent at this instant. Later, at $t = 11.6\,\mu s$ with an apparent chemical reaction, the probabilities of higher fluctuations with a chemical reaction are larger, featured by the higher tail of its p.d.f. At $t = 13.2\,\mu s$, the highly fluctuating events decay, and even the fluctuations with chemical reactions are still larger than those without chemical reactions. The chemical reaction effects on the p.d.f.s are consistent with the conclusions in figure 23.

The evolutions of extreme events during shock compression and free development are investigated by the p.d.f.s without a chemical reaction in figure 25. The evolutions with chemical reactions are similar, and we do not show them for the sake of simplicity. During shock compression, although the averaged viscous dissipation rates are suppressed, the probabilities of extreme events increase, as represented by increasingly higher p.d.f. tails. After shock compression, the probabilities of extreme events begin to decay. Hence, extreme events develop along with shock compression. The main reason is that the shock is located within the mixing regions, and the large velocity gradients around the shock lead to higher viscous dissipation rates. With shock propagating towards the outer side, the extreme events of the viscous dissipation rates become more developed. Later, the extreme events begin to decay without shock located within the mixing regions. The largest fluctuations at different instants are approximately 100 orders of magnitude for the mean values, and these extreme events reveal the intrinsic intermittency of turbulent flows (Yeung *et al.* 2015).

3.5.7. *Spectra and fluxes*

To investigate the scale separations within the mixing regions, we study the spectra of velocity, density and temperature in this section. According to previous analyses of compressible turbulent flows, all of them obey the same power-law solutions with $k^{-5/3}$ in the inertial subrange (Wang, Gotoh & Watanabe 2017*a*; Wang *et al.* 2019; Teng *et al.* 2020). The existence of the inertial subrange with a power-law solution is characteristic of fully developed turbulence (Zhou 2001).

The density and temperature spectra are dependent on circumferential wavenumbers at $t = 12\,\mu s$ during shock compression, at $t = 13.2\,\mu s$ for free development and at $t = 30\,\mu s$ at the late time are exhibited in figure 26. They obey the relation
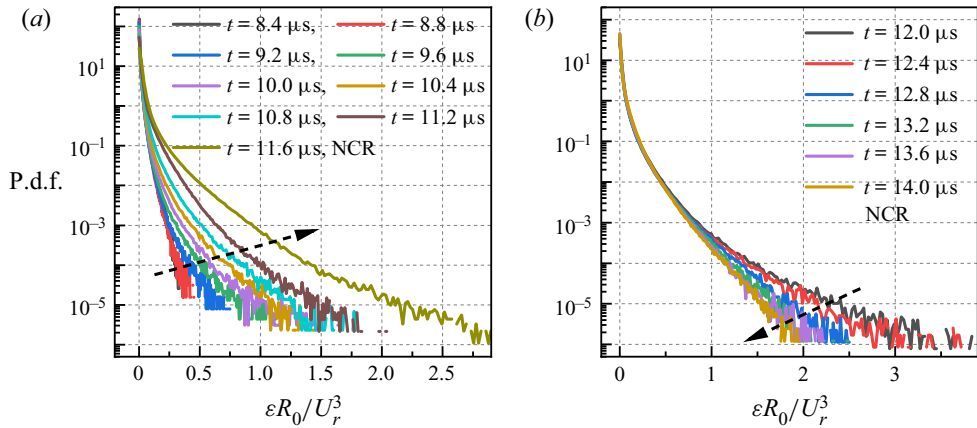
Figure 25. (*a*) Probability distribution functions of the viscous dissipation rates without a chemical reaction during shock compression. (*b*) Probability distribution functions of the viscous dissipation rates without a chemical reaction after shock compression.
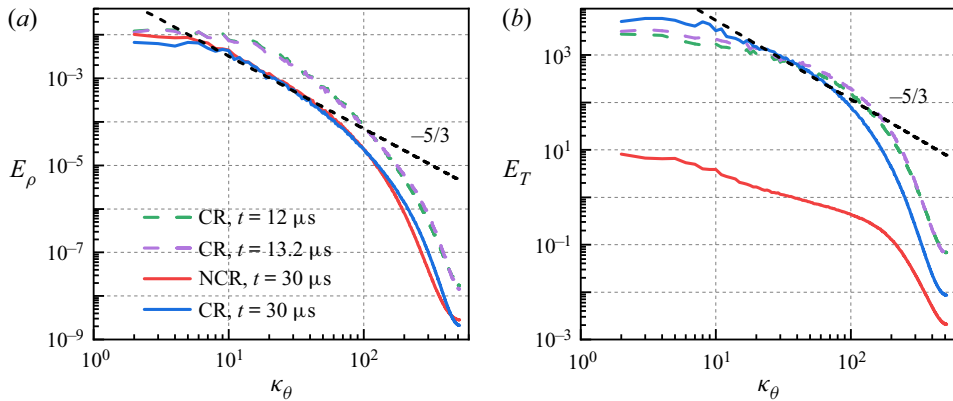

Figure 26. The spectra of fluctuating mixture density (*a*) and temperature (*b*) with and without chemical reactions at $t = 12\,\mu s$, $t = 13.2\,\mu s$ and $t = 30\,\mu s$.

$\int_0^\infty E_X(k_\theta)\,\mathrm{d}k_\theta = \langle X'^2 \rangle$, $\quad E_X(k_\theta) = \int_0^\infty \int_0^\infty \widehat{X'}(k_r, k_\theta, k_z)\widehat{X'}^*(k_r, k_\theta, k_z)\,\mathrm{d}k_r\,\mathrm{d}k_z$. Here, $'$ denotes the fluctuating component, $*$ denotes the complex conjugate, $\hat{}$ denotes the Fourier coefficient, and X denotes ρ for mixture density and T for temperature. For mixture density spectra, the increase in spectral density at high wavenumbers and the decrease in spectral density at low wavenumbers from $t = 12\,\mu s$ to $t = 13.2\,\mu s$ mean that large-scale density cascades to small scales during free development, and then the mixture density spectra begin to decay at all scales. In the late stage the $-5/3$ scaling regions across half a decade are present. Because of the low Reynolds numbers in the present numerical simulations, the inertial subrange with uniform scaling may be short, but the present numerical results also confirm its existence. The chemical reaction effects on the density spectra are represented by high mixture density spectra at high wavenumbers, and this phenomenon is consistent with previous extreme events. For temperature spectra, the development regularity at the early stage is similar to mixture density spectra. Because of the heat release of chemical reactions, the temperature spectra with chemical reactions at low wavenumbers increase with time, and the temperature spectra at high wavenumbers
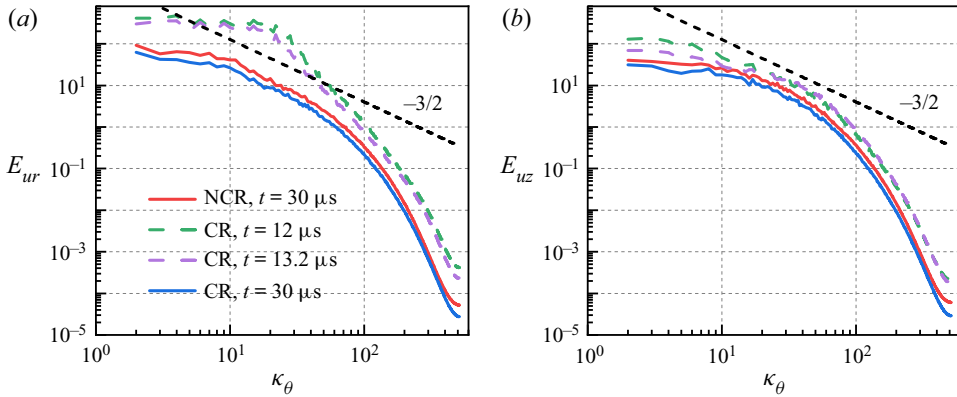
941 A55-28

Figure 27. The spectra of fluctuating radial (*a*) and axial velocity (*b*) with and without chemical reactions at $t = 12\,\mu s$, $t = 13.2\,\mu s$ and $t = 30\,\mu s$.

begin to decay after free development. This means that the non-premixed chemical reaction within the mixing regions provides large-scale heat sources to inject internal energy into the flow field and temperature cascades from large scales to small scales. These temperature transfer routines are similar to forced homogeneous and isotropic turbulence (Wang *et al.* 2019; Yan *et al.* 2020*a,b*), and the inertial subrange with a $-5/3$ scaling over one decade begins to appear in the present numerical simulations. However, the temperature spectra without a chemical reaction would decrease at all scales after free development.

Zhou (2001) proposed that the scaling exponent of kinetic energy should be $-3/2$ for RMI, although the discrepancy from the classic Kolmogorov scaling $-5/3$ is small (Groom & Thornber 2019). We select the same instants of mixture density and temperature to explore the scale separation of radial and axial velocities in figure 27, and their definitions are consistent with density and temperature spectra with $X = u_r$ and $X = u_z$. For radial and axial velocity spectra, inertial subranges are not apparent because of low Reynolds numbers, and their spectra with chemical reactions are small because of higher viscous dissipation rates within the mixing regions at early times. During free development of radial velocity, small scales could not be developed because the radial developments of velocity are constrained by multi-species mixing. This circumstance would be changed for axial velocity with periodic boundary conditions, and small scales can be developed to some extent and then begin to decay.

The inter-scale transfer process of kinetic energy reveals the complexity of compressible turbulent flows, and a filter operation can be employed as a mathematical tool to study the kinetic energy cascade (Wang *et al.* 2013*a*; Zhao, Liu & Lu 2020). We only focus on the inter-scale kinetic energy transfer and rewrite the kinetic energy flux term as

$$\Pi_l^E = -\bar{\rho}\,(\widetilde{uu} - \tilde{u}\tilde{u}) : \nabla\tilde{u}, \qquad (3.20)$$

where $\tilde{u}$ is the Favre-filtered velocity defined as $\tilde{u} = \bar{\rho}u/\bar{\rho}$. In figure 28 we select three typical instants at $t = 12\,\mu s$, $t = 13.2\,\mu s$ and $t = 30\,\mu s$ to explore the kinetic energy cascade across axial scales. During shock compression at $t = 12\,\mu s$, the kinetic energy fluxes at moderate and large scales are negative, which means kinetic energy cascades inversely from small scales to large scales. This phenomenon is consistent with constraint fluctuations during shock compression. The shock compression effects can be explained as kinetic energy transferring from small scales into large scales, and it is more apparent
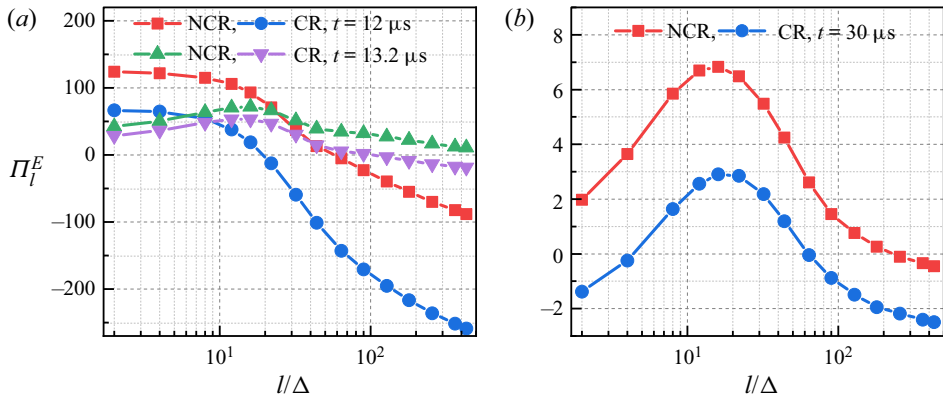
Figure 28. (*a*) The ensemble averages of kinetic energy flux at $t = 12\,\mu\text{s}$ and $t = 13.2\,\mu\text{s}$. (*b*) The ensemble averages of kinetic energy flux at $t = 30\,\mu\text{s}$. Here l is the filter width, and Δ is the grid spacing.

with a chemical reaction. During free development, the backward energy cascade would not be dominant, and there exists a net forward energy cascade from large scales to small scales. In the late time the amplitudes of the kinetic energy cascade decrease, which reflects a weakened nonlinear interaction. The ensemble averages of kinetic energy fluxes with chemical reactions are always smaller than those without chemical reactions, which indicates two intrinsic mechanisms of the chemical reaction. The first is that the chemical reaction weakens the nonlinear interactions with heat release, leading to smaller energy fluxes. The second might be that chemical reactions promote kinetic energy transfer inversely to large scales (Teng *et al.* 2021).

4. Conclusions

The reactive RMI is widely present in the engineering flows, and evolution characteristics of the flow field are different from that without a chemical reaction (Zhou *et al.* 2021). There exists important progress in the past few years, and most of them focus on the planar geometry, two-dimensional numerical simulations or single-step chemical kinetic mechanisms (Attal & Ramaprabhu 2015; Attal *et al.* 2015; Bambauer *et al.* 2020, 2021). The regulations should be extended to some practical applications, and we carry out three-dimensional DNS with multi-mode perturbations and a detailed chemical mechanism of the cylindrical geometry in this paper. For the element chemical reaction of non-premixed hydrogen and oxygen, 9-species and 19-reaction models are adopted. The chemical reaction effects on the process of transition and late-time turbulent mixing are highlighted to uncover the temporal evolution of RMI with heat release and combustion wave propagation. The complex interactions of shock and chemical reaction lead to a quick growth of the mixing width and weakened turbulent mixing. They are reflected on different positions within the mixing regions, which means that the combustion wave promotes the boundary development of the mixing regions and heat release weakens the turbulent mixing around the centre of the mixing regions. With time after the second reshock, the turbulent mixing would decay and the chemical reaction would be dominant in the late stage. Hence, the eventual mixing is suppressed by the chemical reaction.

To study the process of transition and turbulent mixing, we employ multi-mode initial interfacial perturbation. Our numerical results reveal that the similarity exponent of shock propagation is consistent with theoretical prediction, the Taylor Reynolds number is large

enough for fully developed turbulent flows, and the grid resolution is small enough to capture the Kolmogorov viscous length scales. All of these results assure the reliable accuracy of the present numerical simulations.

We proposed a new definition of mixing width for more-species chemical reactions, which involved all elements of all species. The evolutions of the inner radius of mixing regions with and without chemical reactions are nearly the same, while the outer radii are different. Because of non-premixed combustion and combustion wave propagation, the growth rate of the outer radial with a chemical reaction is larger. The heat release results in a larger temperature gradient around the outer radius, and it promotes the growth of the mixing width.

Sufficient energy is needed for the occurrence of the chemical reaction, and it absorbs energy from the flow field in the early times. Nevertheless, the total internal energy within the mixing regions increases over time. The main reason lies in the fact that the change of the internal energy induced by the propagating shock wave is much larger than that induced by the chemical reaction, under the present thermodynamic conditions. After reshock, the fuller mixing of fuels and oxygen leads to a drastic chemical reaction, and their discrepancies in the mixing characteristics and turbulent statistics begin to be apparent. The fuller chemical reaction is reflected in the large heat release rate, large production and consumption rate. Because of the smaller scales of spike distribution, the chemical reaction occurs mainly within the mixing regions, and tends to happen towards the spikes. The highlighted statistical variables within the mixing regions mainly include turbulent kinetic energy, enstrophy, helicity, viscous dissipation rate, palinstrophy, skewness, flatness, spectra and inter-scale fluxes. Because of the heat release of the chemical reaction, the fluctuating radial velocity is smaller, and the corresponding decay rate is larger in the late time. After reshock, the enstrophy and helicity begin to develop gradually, while chemical reactions hinder the development process. The development of helicity after reshock might be regarded as the transition mark in the present three-dimensional cylindrical RMI because the strong three-dimensional instability comes from quasi-two-dimensional perturbations. The palinstrophy is related to the viscous dissipation of enstrophy and skewness, and we can prove that compressibility does not affect the viscous dissipation of enstrophy in compressible flows. The developments of small-scale structures with chemical reactions after reshock are weakened, but the high-order moments are fully developed later by removing the main shock wave.

The above physical process descriptions can be attributed to the multiple shock effects locally, and the physical regulations obtained in the cylindrical geometry is similar to that in the planar geometry. We carried out DNS of RMI with reshock and a chemical reaction in the planar geometry, and the numerical setting is consistent with the shock tube facility at Los Alamos National Laboratory (Balakumar *et al.* 2008; Orlicz *et al.* 2009; Balakumar *et al.* 2012; Tomkins *et al.* 2008, 2013) in the Appendix A. The accelerated growth of the mixing width induced by the generated combustion wave is varied after the reshock and before the rarefaction wave. The weakened turbulent mixing is validated by the larger decaying rate of turbulent kinetic energy before reshock. More specific details have been given in the Appendix A.

We compare the spectra and inter-scale fluxes with and without chemical reactions to differ their multiscale characteristics. After reshock, the spectral densities at high wavenumbers begin to develop and then decay. While the spectral densities at low wavenumbers decay over time. Hence, there exists a time range of the developments of small-scale structures. The spectra of thermal variables, such as density and temperature, show apparent inertial subranges, while the inertial subranges of velocity spectra are not apparent because of the low Reynolds number in the present numerical simulations.

The amplitudes of the multiscale distributions of velocity fields with chemical reactions are smaller than those without chemical reactions. For the temperature spectra, the amplitudes with chemical reactions are larger because of heat release. The shock compression corresponds to an inverse energy cascade, which is strengthened by a chemical reaction. Then, the amplitudes of kinetic energy fluxes with chemical reactions are always smaller than those without chemical reactions, which reflects the weakened nonlinear interactions and promotes the process of the inverse energy cascade.

To summarize, we perform three-dimensional DNS of cylindrical RMI with and without chemical reactions and uncover the chemical reaction effects on the transition and late-time turbulent mixing. The growth of the mixing width is promoted by the chemical reaction because of combustion wave propagation, and turbulent mixing is weakened by the chemical reaction because of heat release.

Author ORCIDs.
- ⓘ Zheng Yan https://orcid.org/0000-0002-8813-3216;
- ⓘ Yaowei Fu https://orcid.org/0000-0001-9261-252X;
- ⓘ Changping Yu https://orcid.org/0000-0002-2126-1344.

Appendix A. DNS of RMI with a chemical reaction in a planar geometry

We carry out DNS of RMI with a chemical reaction in a planar geometry to illustrate the chemical reaction effect on the mixing transition and turbulent statistics. The initial configurations are exhibited schematically in figure 29. The cross-section length is 20 mm, and the streamwise length is 137 mm, which is consistent with the shock tube facility at Los Alamos National Laboratory (Balakumar *et al.* 2008; Orlicz *et al.* 2009; Tomkins *et al.* 2008, 2013; Balakumar *et al.* 2012). The initial perturbed interface centre locates at $x = 0$ m, and the initial shock wave locates at $x = 0.005$ m. To avoid the reflected shock effect, we adopt a buffer region adjoint to the left main computational domain with a stretched grid. The amplitude of the initial perturbed interface is determined by a power spectrum method (Thornber *et al.* 2010, 2017), and it can be expressed as

$$A(y, z) = \sum_{m,n=0}^{N} a_{m,n} \cos(k_0 m y) \cos(k_0 n z) + b_{m,n} \cos(k_0 m y) \sin(k_0 n z)$$
$$+ c_{m,n} \sin(k_0 m y) \cos(k_0 n z) + d_{m,n} \sin(k_0 m y) \sin(k_0 n z), \quad (A1)$$

where $k_0 = 2\pi/L$, L is the length of the cross-section, and m and n are the perturbed modes in the y and z directions, respectively. Other details refer to a previous valuable paper (Thornber *et al.* 2017). In our numerical simulations the perturbed mode ranges from 8 to 32, and 256 grid cells are used in the cross-section. According to our previous
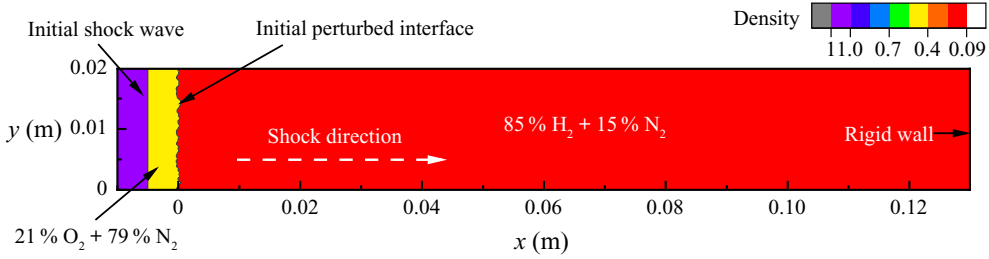
Figure 29. The initial computational configurations of the planar geometry.

Geometry	M_s	Computational domains (m)	Grid resolution	Pre-shock temperature (K)
Planar	1.5	$[-0.01, 0.137] \times [0, 0.02] \times [0, 0.02]$	$1882 \times 256 \times 256$	800

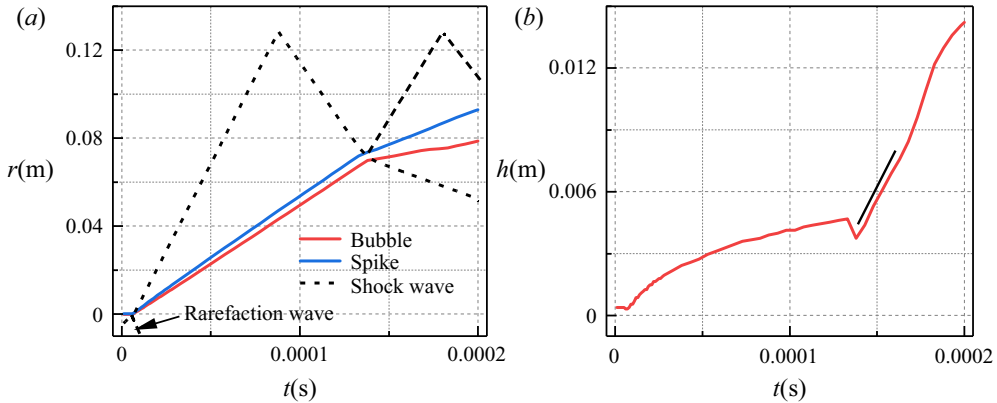Table 2. Initial parameter settings of the planar geometry.

Figure 30. (*a*) Displacement of the bubbles, spikes and shock wave of the planar geometry. (*b*) The mixing width over time of the planar geometry.

conclusion, the heat released by the chemical reaction decreases the needed grid number to resolve the Kolmogorov scale. Other initial parameter settings are listed in table 2.

The determination method of the bubble and spike positions of the planar geometry is consistent with that of the cylindrical geometry. To be mentioned, we adopt a plane-averaged approach to obtain the mean physical variable $\langle a(x) \rangle$ as

$$\langle a(x) \rangle = \frac{1}{\iint dy\,dz} \iint a(x, y, z)\,dy\,dz. \tag{A2}$$

We show the displacement of the bubbles, spikes and shock wave in figure 30(*a*). From the beginning, the shock wave propagates along the streamwise direction, and then interacts with the perturbed interface for the first time. A rarefaction wave is generated and propagates in an opposite direction. In the meantime, a transmitted shock wave propagates in the streamwise direction until the right rigid wall. The shocked perturbed interface would move along the streamwise direction, and interact with the reshock subsequently. The mixing width evolutions are shown in figure 30(*b*), the growth of the mixing width
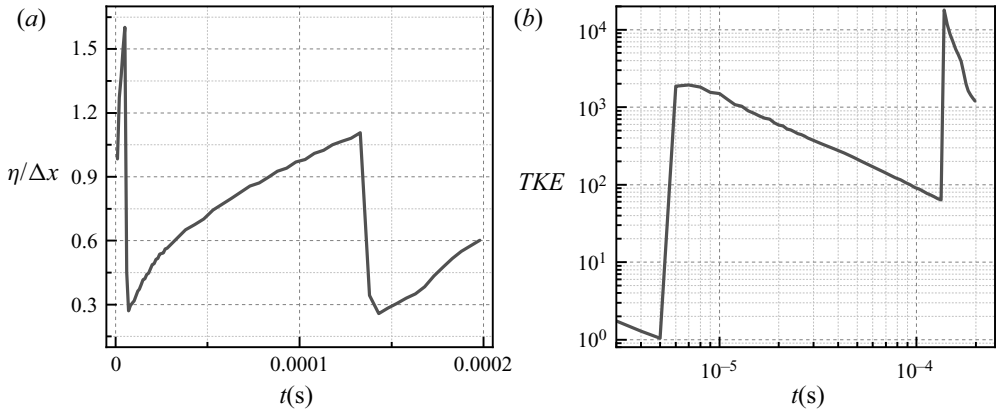
Figure 31. (*a*) The ratio of the Kolmogorov scale and grid spacing over time of the planar geometry. (*b*) The turbulent kinetic energy of the planar geometry.
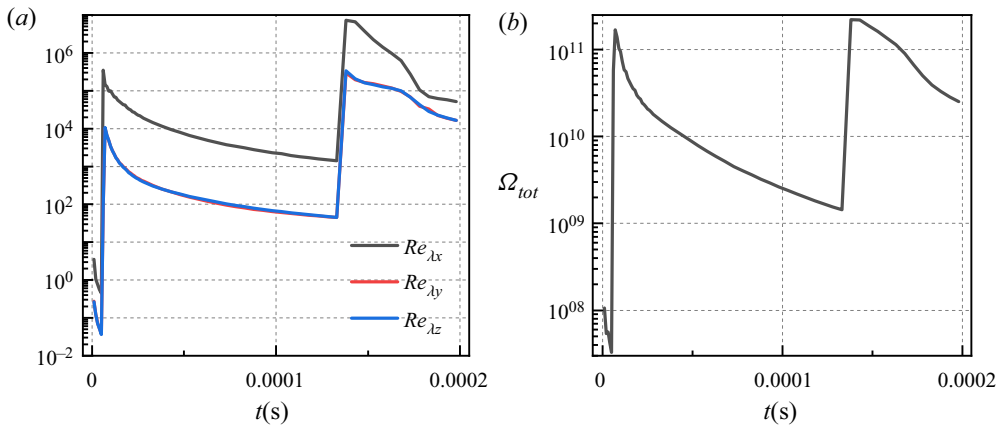

Figure 32. (*a*) Taylor Reynolds numbers over time of the planar geometry. (*b*) The enstrophy over time of the planar geometry.

after the reshock is linear, and it is consistent with the linear reshock model (Mikaelian 1989). After the linear growth of the mixing width, we found that the mixing width is re-accelerated, and it may originate from the promoting effect of the generated combustion wave.

We show the ratio of the Kolmogorov scale and grid spacing over time in figure 31(*a*), and the ratios are larger than 0.5 except around the times with shock and reshock. The shock itself leads to a large velocity gradient, and may induce additional viscosity dissipation. Hence, the current grid resolution is sufficient to obtain the following highlighted parameters. In figure 31(*b*) we show the turbulent kinetic energy over time. Every shock corresponds to a huge increase of turbulent kinetic energy. Before the reshock, the turbulent kinetic energy decays self-similarly with a decay exponent $\theta \approx 1.17$. After the reshock, the decay rate is larger. The larger decay rate may partly originate from the apparent chemical reaction after the reshock. Because of the limit of the shock tube length, the reflected shock wave after the first reshock would interact with the perturbed interface repeatedly. In contrast to the cylindrical geometry without any wall, the

941 A55-34

development of the perturbed interface is affected by multiple shocks, and the self-similar decay exponent is hard to obtain.

The directional Taylor Reynolds numbers are shown in figure 32(*a*). All directional Taylor Reynolds numbers are larger than 100–140, and they satisfy the transition criteria (Dimotakis 2000; Zhou *et al.* 2019). The temporal evolution of the directional Taylor Reynolds numbers is similar to that in the shock tube facility (Balakumar *et al.* 2008; Orlicz *et al.* 2009; Balakumar *et al.* 2012). However, they are larger than that of the cylindrical geometry. The main reason may lie in a larger Taylor microscale of the planar geometry. The discrepancy may also originate from the initial perturbations, the convergent geometry effect, etc. The enstrophy evolution in figure 32(*b*) is similar to the trend of the directional Taylor Reynolds numbers.

REFERENCES

ABARZHI, S.I., BHOWMICK, A.K., NAVEH, A., PANDIAN, A., SWISHER, N.C., STELLINGWERF, R.F. & ARNETT, W.D. 2019 Supernova, nuclear synthesis, fluid instabilities, and interfacial mixing. *Proc. Natl Acad. Sci. USA* **116**, 18184–18192.

ALMGREN, A.S., BELL, J.B., RENDLEMAN, C.A. & ZINGALE, M. 2006 Low mach number modeling of type Ia supernovae. I. Hydrodynamics. *Astrophys J.* **637**, 922–936.

ANDERSON, J.D. 2010 *Fundamentals of Aerodynamics*. Tata McGraw-Hill Education.

ATTAL, N. & RAMAPRABHU, P. 2015 Numerical investigation of a single-mode chemically reacting Richtmyer–Meshkov instability. *Shock Waves* **25**, 307–328.

ATTAL, N., RAMAPRABHU, P., HOSSAIN, J., KARKHANIS, V., UDDIN, M., GORD, J.R. & ROY, S. 2015 Development and validation of a chemical reaction solver coupled to the flash code for combustion applications. *Comput. Fluids* **107**, 59–76.

BALAKUMAR, B.J., ORLICZ, G.C., RISTORCELLI, J.R., BALASUBRAMANIAN, S., PRESTRIDGE, K.P. & TOMKINS, C.D. 2012 Turbulent mixing in a Richtmyer–Meshkov fluid layer after reshock: velocity and density statistics. *J. Fluid Mech.* **696**, 67–93.

BALAKUMAR, B.J., ORLICZ, G.C., TOMKINS, C.D. & PRESTRIDGE, K.P. 2008 Simultaneous particle-image velocimetry–planar laser-induced fluorescence measurements of Richtmyer–Meshkov instability growth in a gas curtain with and without reshock. *Phys. Fluids* **20**, 124103.

BAMBAUER, M., CHAKRABORTY, N., KLEIN, M. & HASSLBERGER, J. 2021 Vortex dynamics and fractal structures in reactive and nonreactive Richtmyer–Meshkov instability. *Phys. Fluids* **33**, 044114.

BAMBAUER, M., HASSLBERGER, J. & KLEIN, M. 2020 Direct numerical simulation of the Richtmyer–Meshkov instability in reactive and nonreactive flows. *Combust. Sci. Technol.* **192**, 2010–2027.

BATCHELOR, G.K. & TOWNSEND, A.A. 1947 Decay of vorticity in isotropic turbulence. *Proc. R. Soc.* A **191**, 534–550.

BELL, G.I. 1951 Taylor instability on cylinders and spheres in the small amplitude approximation. *Tech. Rep.* LA-1321. Los Alamos National Laboratory.

BENDER, J.D., *et al.* 2021 Simulation and flow physics of a shocked and reshocked high-energy-density mixing layer. *J. Fluid Mech.* **915**, A84.

BENGOECHEA, S., STEIN, L., REISS, J. & SESTERHENN, J. 2014 Numerical investigation of reactive and non-reactive Richtmyer–Meshkov instabilities. In *Active Flow and Combustion Control 2014* (ed. K. Rudibert), pp. 343–361. Springer.

BILLET, G. 2005 Improvement of convective concentration fluxes in a one step reactive flow solver. *J. Comput. Phys.* **204**, 319–352.

BROUILLETTE, M. 2002 The Richtmyer–Meshkov instability. *Annu. Rev. Fluid Mech.* **34**, 445–468.

BUDZINSKI, J.M., BENJAMIN, R.F. & JACOBS, J.W. 1994 Influence of initial conditions on the flow patterns of a shock-accelerated thin fluid layer. *Phys. Fluids* **6**, 3510–3512.

CHERTKOV, M., LEBEDEV, V. & VLADIMIROVA, N. 2009 Reactive Rayleigh–Taylor turbulence. *J. Fluid Mech.* **633**, 1–16.

CHISNELL, R.F. 1998 An analytic description of converging shock waves. *J. Fluid Mech.* **354**, 357–375.

COOK, A.W. & ZHOU, Y. 2002 Energy transfer in Rayleigh–Taylor instability. *Phys. Rev.* E **66**, 026312.

DEBUE, P., VALORI, V., CUVIER, C., DAVIAUD, F., FOUCAUT, J.M., LAVAL, J.P., WIERTEL, C., PADILLA, V. & DUBRULLE, B. 2021 Three-dimensional analysis of precursors to non-viscous dissipation in an experimental turbulent flow. *J. Fluid Mech.* **914**, A9.

DIMONTE, G. & SCHNEIDER, M. 2000 Density ratio dependence of Rayleigh–Taylor mixing for sustained and impulsive acceleration histories. *Phys. Fluids* **12**, 304–321.

DIMOTAKIS, P.E. 2000 The mixing transition in turbulent flow. *J. Fluid Mech.* **409**, 69–98.

DIMOTAKIS, P.E. & SAMTANEY, R. 2006 Planar shock cylindrical focusing by a perfect-gas lens. *Phys. Fluids* **18**, 031705.

DING, J., LI, J., SUN, R., ZHAI, Z. & LUO, X. 2019 Convergent Richtmyer–Meshkov instability of a heavy gas layer with perturbed outer interface. *J. Fluid Mech.* **878**, 277–291.

DYKE, M.V. & GUTTMANN, A.J. 1982 The converging shock wave from a spherical or cylindrical piston. *J. Fluid Mech.* **120**, 451–462.

EYINK, G.L. & DRIVAS, T.D. 2018 Cascades and dissipative anomalies in compressible fluid turbulence. *Phys. Rev. X* **8**, 011022.

FU, Y., YU, C. & LI, X. 2020 Energy transport characteristics of converging Richtmyer–Meshkov instability. *AIP Adv.* **10**, 105302.

FU, Y., YU, C., YAN, Z. & LI, X. 2019a DNS analysis of the effects of combustion on turbulence in a supersonic H2/air jet flow. *Aerosp. Sci. Technol.* **93**, 105362.

FU, Y., YU, C., YAN, Z. & LI, X. 2019b The effects of combustion on turbulent statistics in a supersonic turbulent jet. *Adv. Appl. Math. Mech.* **11**, 664–674.

GATSKI, T.B. & BONNET, J.P. 2013 *Compressibility, Turbulence and High Speed Flow*. Academic Press.

GAUTHIER, S. 2017 Compressible Rayleigh–Taylor turbulent mixing layer between newtonian miscible fluids. *J. Fluid Mech.* **830**, 211–256.

GORDON, S. & MCBRIDE, B.J. 1971 Computer program for calculation of complex chemical equilibrium compositions, rocket performance, incident and reflected shocks and Chapman-Jouguet detonations. *Tech. Rep.* SF-273. NASA.

GRAVES, R.E. & ARGROW, B.M. 1999 Bulk viscosity: past to present. *J. Thermophys. Heat Transfer* **13**, 337–342.

GROOM, M. & THORNBER, B. 2019 Direct numerical simulation of the multimode narrowband Richtmyer–Meshkov instability. *Comput. Fluids* **194**, 104309.

GROOM, M. & THORNBER, B. 2020 The influence of initial perturbation power spectra on the growth of a turbulent mixing layer induced by Richtmyer–Meshkov instability. *Physica D* **407**, 132463.

GROOM, M. & THORNBER, B. 2021 Reynolds number dependence of turbulence induced by the Richtmyer–Meshkov instability using direct numerical simulations. *J. Fluid Mech.* **908**, A31.

GUDERLEY, K.G. 1942 Starke kugelige und zylindrische verdichtungsstosse in der nahe des kugelmittelpunktes bzw. der zylinderachse. *Luftfahrtforschung* **19**, 302–312.

HILL, D.J., PANTANO, C. & PULLIN, D.I. 2006 Large-eddy simulation and multiscale modelling of a Richtmyer–Meshkov instability with reshock. *J. Fluid Mech.* **557**, 29–61.

HOUAS, L. & CHEMOUNI, I. 1996 Experimental investigation of Richtmyer–Meshkov instability in shock tube. *Phys. Fluids* **8**, 614–627.

HUANG, M.J. & LEONARD, A. 1994 Power-law decay of homogeneous turbulence at low Reynolds numbers. *Phys. Fluids* **6**, 3765–3775.

JIANG, H., DONG, G., CHEN, X. & LI, B. 2016a A parameterization of the Richtmyer–Meshkov instability on a premixed flame interface induced by the successive passages of shock waves. *Combust. Flame* **169**, 229–241.

JIANG, H., DONG, G. & WU, J.T. 2016b Numerical simulations of the process of multiple shock–flame interactions. *Acta Mech. Sin.* **32**, 659–669.

KÁRMÁN, T. & HOWARTH, L. 1938 On the statistical theory of isotropic turbulence. *Proc. R. Soc. Lond.* A **164**, 192–215.

KEE, R.J., RUPLEY, F.M. & MILLER, J.A. 1989 Chemkin-II: a Fortran chemical kinetics package for the analysis of gas-phase chemical kinetics. *Tech. Rep.* SAND89-8009. Sandia National Laboratories.

KHOKHLOV, A.M., ORAN, E.S., CHTCHELKANOVA, A.Y. & WHEELERC, J.C. 1999 Interaction of a shock with a sinusoidally perturbed flame. *Combust. Flame* **117**, 99–116.

KILCHYK, V., NALIM, R. & MERKLE, C. 2011 Laminar premixed flame fuel consumption rate modulation by shocks and expansion waves. *Combust. Flame* **158**, 1140–1148.

LEINOV, E., MALAMUD, G., ELBAZ, Y., LEVIN, L.A., BEN-DOR, G., SHVARTS, D. & SADOT, O. 2009 Experimental and numerical investigation of the Richtmyer–Meshkov instability under reshock conditions. *J. Fluid Mech.* **626**, 449–112.

LESIEUR, M. 1997 *Turbulence in Fluids*. Kluwer Academic.

LI, X., FU, Y., YU, C. & LI, L. 2021 Statistical characteristics of turbulent mixing in spherical and cylindrical converging Richtmyer–Meshkov instabilities. *J. Fluid Mech.* **928**, A10.

LI, X., LENG, Y. & HE, Z. 2013 Optimized sixth-order monotonicity-preserving scheme by nonlinear spectral analysis. *Intl J. Numer. Meth. Fluids* **73**, 560–577.

LI, J., ZHAO, Z., KAZAKOV, A. & DRYER, F.L. 2004 An updated comprehensive kinetic model of hydrogen combustion. *Intl J. Chem. Kinet.* **36**, 566–575.

LINDL, J., LANDEN, O., EDWARDS, J., MOSES, E. & TEAM, N. 2014 Review of the national ignition campaign 2009–2012. *Phys. Plasmas* **21**, 020501.

LIU, W., YU, C., YE, W., WANG, L. & HE, X. 2014 Nonlinear theory of classical cylindrical Richtmyer–Meshkov instability for arbitrary Atwood numbers. *Phys. Plasmas* **21**, 062119.

LOMBARDINI, M., HILL, D.J., PULLIN, D.I. & MEIRON, D.I. 2011 Atwood ratio dependence of Richtmyer–Meshkov flows under reshock conditions using large-eddy simulations. *J. Fluid Mech.* **670**, 439–480.

LOMBARDINI, M. & PULLIN, D.I. 2009 Small-amplitude perturbations in the three-dimensional cylindrical Richtmyer–Meshkov instability. *Phys. Fluids* **21**, 114103.

LOMBARDINI, M., PULLIN, D. & MEIRON, D. 2012 Transition to turbulence in shock-driven mixing: a Mach number study. *J. Fluid Mech.* **690**, 203–226.

LOMBARDINI, M., PULLIN, D. & MEIRON, D. 2014a Turbulent mixing driven by spherical implosions. Part 1. Flow description and mixing-layer growth. *J. Fluid Mech.* **748**, 85–112.

LOMBARDINI, M., PULLIN, D. & MEIRON, D. 2014b Turbulent mixing driven by spherical implosions. Part 2. Turbulence statistics. *J. Fluid Mech.* **748**, 113–142.

LUO, X., DING, J., WANG, M., ZHAI, Z. & SI, T. 2015 A semi-annular shock tube for studying cylindrically converging Richtmyer–Meshkov instability. *Phys. Fluids* **27**, 091702.

LUO, X., SI, T., YANG, J. & ZHAI, Z. 2014 A cylindrical converging shock tube for shock-interface studies. *Rev. Sci. Instrum.* **85**, 015107.

MASSA, L. & JHA, P. 2012 Linear analysis of the Richtmyer–Meshkov instability in shock-flame interactions. *Phys. Fluids* **24**, 056101.

MCFARLAND, J., REILLY, D., CREEL, S., MCDONALD, C., FINN, T. & RANJAN, D. 2014 Experimental investigation of the inclined interface Richtmyer–Meshkov instability before and after reshock. *Exp. Fluids* **55**, 1–14.

MESHKOV, E.E. 1969 Instability of the interface of two gases accelerated by a shock wave. *Fluid Dyn.* **43**, 101–104.

MIKAELIAN, K.O. 1989 Turbulent mixing generated by Rayleigh–Taylor and Richtmyer–Meshkov instabilities. *Physica* D **36**, 343–357.

MIKAELIAN, K.O. 2005 Rayleigh–Taylor and Richtmyer–Meshkov instabilities and mixing in stratified cylindrical shells. *Phys. Fluids* **17**, 094105.

MIKAELIAN, K.O. & OLSON, B.J. 2020 On modeling Richtmyer–Meshkov turbulent mixing widths. *Physica* D **402**, 132243.

MOFFATT, H.K. 2021 Extreme events in turbulent flow. *J. Fluid Mech.* **914**, F1.

MOFFATT, H.K. & TSINOBER, A. 1992 Helicity in laminar and turbulence flow. *Annu. Rev. Fluid Mech.* **24**, 281–312.

MOTL, B., OAKLEY, J., RANJAN, D., WEBER, C. & ANDERSON, M. 2009 Experimental validation of a Richtmyer–Meshkov scaling law over large density ratio and shock strength ranges. *Phys. Fluids* **21**, 126102.

ORLICZ, G.C., BALAKUMAR, B.J., TOMKINS, C.D. & PRESTRIDGE, K.P. 2009 A Mach number study of the Richtmyer–Meshkov instability in a varicose, heavy-gas curtain. *Phys. Fluids* **21**, 064102.

ORSZAG, S.A. 1977 Statistical theory of turbulence. In *Fluid Dynamics 1973, Les Houches Summer School of Theoretical Physics* (ed. R. Balian & J.L. Peube), pp. 237–374. Gordon and Breach.

PLESSET, M.S. 1954 On the stability of fluid flows with spherical symmetry. *J. Appl. Phys.* **25**, 96–98.

POPE, S.B. 2010 *Turbulent Flows*. Combridge University Press.

POUQUET, A., LESIEUR, M., ANDRÉ, J.C. & BASDEVANT, C. 1975 Evolution of high Reynolds number two-dimensional turbulence. *J. Fluid Mech.* **72**, 305–319.

RAMAPRABHU, P., DIMONTE, G., WOODWARD, P., FRYER, C., ROCKEFELLER, G., MUTHURAMAN, K., LIN, P.H. & JAYARAJ, J. 2012 The late-time dynamics of the single-mode Rayleigh–Taylor instability. *Phys. Fluids* **24**, 074107.

RICHTMYER, R.D. 1960 Taylor instability in shock acceleration of compressible fluids. *Commun. Pure Appl. Maths* **13**, 297–319.

ROBEY, H.F., ZHOU, Y., BUCKINGHAM, A.C., KEITER, P., REMINGTON, B.A. & DRAKE, R.P. 2003 The time scale for the transition to turbulence in a high Reynolds number, accelerated flow. *Phys. Plasmas* **10**, 614–622.

SAFFMAN, P.G. 1967 The large-scale structure of homogeneous turbulence. *J. Fluid Mech.* **27**, 581–593.

SAHOO, G., BONACCORSO, F. & BIFERALE, L. 2015 Role of helicity for large- and small-scale turbulent fluctuations. *Phys. Rev.* E **92**, 051002.

SAMTANEY, R., PULLIN, D.I. & KOSOVIÉ, B. 2001 Direct numerical simulation of decaying compressible turbulence and shocklet statistics. *Phys. Fluids* **13**, 1415–1430.

SI, T., LONG, T., ZHAI, Z. & LUO, X. 2015 Experimental investigation of cylindrical converging shock waves interacting with a polygonal heavy gas cylinder. *J. Fluid Mech.* **784**, 225–251.

TENG, J., WANG, J., LI, H. & CHEN, S. 2020 Spectra and scaling in chemically reacting compressible isotropic turbulence. *Phys. Rev. Fluids* **5**, 084601.

TENG, J., WANG, J., LI, H. & CHEN, S. 2021 Interscale kinetic energy transfer in chemically reacting compressible isotropic turbulence. *J. Fluid Mech.* **912**, A36.

THORNBER, B., et al. 2017 Late-time growth rate, mixing, and anisotropy in the multimode narrowband Richtmyer–Meshkov instability: the θ-group collaboration. *Phys. Fluids* **29**, 105107.

THORNBER, B., DRIKAKIS, D., YOUNGS, D.L. & WILLIAMS, R.J.R. 2010 The influence of initial conditions on turbulent mixing due to Richtmyer–Meshkov instability. *J. Fluid Mech.* **654**, 99–139.

TOMKINS, C.D., BALAKUMAR, B.J., ORLICZ, G., PRESTRIDGE, K.P. & RISTORCELLI, J.R. 2013 Evolution of the density self-correlation in developing Richtmyer–Meshkov turbulence. *J. Fluid Mech.* **735**, 288–306.

TOMKINS, C.D., KUMAR, S., ORLICZ, G.C. & PRESTRIDGE, K.P. 2008 An experimental investigation of mixing mechanisms in shock-accelerated flow. *J. Fluid Mech.* **611**, 131–150.

TRAN, C.V. & DRITSCHEL, D.G. 2006 Vanishing enstrophy dissipation in two-dimensional Navier–Stokes turbulence in the inviscid limit. *J. Fluid Mech.* **559**, 107–116.

TRITSCHLER, V.K., ZUBEL, M., HICKEL, S. & ADAMS, N.A. 2014 Evolution of length scales and statistics of Richtmyer–Meshkov instability from direct numerical simulations. *Phys. Rev.* E **90**, 063001.

VANDENBOOMGAERDE, M. & AYMARD, C. 2011 Analytical theory for planar shock focusing through perfect gas lens and shock tube experiment designs. *Phys. Fluids* **23**, 016101.

VANDENBOOMGAERDE, M., SOUFFLAND, D., MARIANI, C., BIAMINO, L., JOURDAN, G. & HOUAS, L. 2014 An experimental and numerical investigation of the dependency on the initial conditions of the Richtmyer–Meshkov instability. *Phys. Fluids* **26**, 024109.

VETTER, M. & STURTEVANT, B. 1995 Experiments on the Richtmyer–Meshkov instability of an air/SF6 interface. *Shock Waves* **4**, 247–252.

WANG, L., et al. 2017b Theoretical and simulation research of hydrodynamic instabilities in inertial-confinement fusion implosions. *Sci. China: Phys. Mech. Astron.* **60**, 055201.

WANG, J., GOTOH, T. & WATANABE, T. 2017a Spectra and statistics in compressible isotropic turbulence. *Phys. Rev. Fluids* **2**, 013403.

WANG, J., WAN, M., CHEN, S., XIE, C., WANG, L. & CHEN, S. 2019 Cascades of temperature and entropy fluctuations in compressible turbulence. *J. Fluid Mech.* **867**, 195–215.

WANG, L., WU, J., GUO, H., YE, W., LIU, J., ZHANG, W. & HE, X. 2015 Weakly nonlinear Bell–Plesset effects for a uniformly converging cylinder. *Phys. Plasmas* **22**, 082702.

WANG, L., WU, J., YE, W., ZHANG, W. & HE, X. 2013b Weakly nonlinear incompressible Rayleigh–Taylor instability growth at cylindrically convergent interfaces. *Phys. Plasmas* **20**, 042708.

WANG, J., YANG, Y., SHI, Y., XIAO, Z., HE, X. & CHEN, S. 2013a Cascade of kinetic energy in three-dimensional compressible turbulence. *Phys. Rev. Lett.* **110**, 214505.

WU, J., LIU, H. & XIAO, Z. 2021 Refined modelling of the single-mode cylindrical Richtmyer–Meshkov instability. *J. Fluid Mech.* **908**, A9.

YAN, Z., LI, X., WANG, J. & YU, C. 2019 Effect of pressure on joint cascade of kinetic energy and helicity in compressible helical turbulence. *Phys. Rev.* E **99**, 033114.

YAN, Z., LI, X.L., YU, C.P. & WANG, J.C. 2020a Cross-chirality transfer of kinetic energy and helicity in compressible helical turbulence. *Phys. Rev. Fluids* **5**, 084604.

YAN, Z., LI, X.L., YU, C.P., WANG, J.C. & CHEN, S.Y. 2020b Dual channels of helicity cascade in turbulent flows. *J. Fluid Mech.* **894**, R2.

YEUNG, P.K., ZHAI, X.M. & SREENIVASAN, K.R. 2015 Extreme events in computational turbulence. *Proc. Natl Acad. Sci. USA* **112**, 12633–12638.

YOUNGS, D.L. 2013 The density ratio dependence of self-similar Rayleigh–Taylor mixing. *Phil. Trans. R. Soc.* A **371**, 20120173.

ZHAI, Z., LIU, C., QIN, F., YANG, J. & LUO, X. 2010 Generation of cylindrical converging shock waves based on shock dynamics theory. *Phys. Fluids* **22**, 041701.

ZHAI, Z., SI, T., LUO, X., YANG, J., LIU, C., TAN, D. & ZOU, L. 2012 Parametric study of cylindrical converging shock waves generated based on shock dynamics theory. *Phys. Fluids* **24**, 026101.

ZHAI, Z., ZOU, L., WU, Q. & LUO, X. 2018 Review of experimental Richtmyer–Meshkov instability in shock tube: from simple to complex. *Proc. Inst. Mech. Engrs* C **232**, 2830–2849.

ZHANG, Y., RUAN, Y., XIE, H. & TIAN, B. 2020 Mixed mass of classical Rayleigh–Taylor mixing at arbitrary density ratios. *Phys. Fluids* **22**, 011702.

ZHAO, Z., LIU, N.S. & LU, X.Y. 2020 Kinetic energy and enstrophy transfer in compressible Rayleigh–Taylor turbulence. *J. Fluid Mech.* **904**, A37.

ZHOU, Y. 2001 A scaling analysis of turbulent flows driven by Rayleigh–Taylor and Richtmyer–Meshkov instabilities. *Phys. Fluids* **13**, 538–543.

ZHOU, Y. 2007 Unification and extension of the concepts of similarity criteria and mixing transition for studying astrophysics using high energy density laboratory experiments or numerical simulations. *Phys. Plasmas* **14**, 082701.

ZHOU, Y. 2017a Rayleigh–Taylor and Richtmyer–Meshkov instability induced flow, turbulence, and mixing. I. *Phys. Rep.* **720–722**, 1–136.

ZHOU, Y. 2017b Rayleigh–Taylor and Richtmyer–Meshkov instability induced flow, turbulence, and mixing. II. *Phys. Rep.* **723–725**, 1–160.

ZHOU, Y., CABOT, W.H. & THORNBER, B. 2016 Asymptotic behavior of the mixed mass in Rayleigh–Taylor and Richtmyer–Meshkov instability induced flows. *Phys. Plasmas* **23**, 052712.

ZHOU, Y., CLARK, T.T., CLARK, D.S., GLENDINNING, S.G., SKINNER, M.A., HUNTINGTON, C.M., HURRICANE, O.A., DIMITS, A.M. & REMINGTON, B.A. 2019 Turbulent mixing and transition criteria of flows induced by hydrodynamic instabilities. *Phys. Plasmas* **26**, 080901.

ZHOU, Y., GROOM, M. & THORNBER, B. 2020 Dependence of enstrophy transport and mixed mass on dimensionality and initial conditions in the Richtmyer–Meshkov instability induced flows. *Trans. ASME J. Fluids Engng* **142**, 121104.

ZHOU, Y., *et al.* 2003 Progress in understanding turbulent mixing induced by Rayleigh–Taylor and Richtmyer–Meshkov instabilities. *Phys. Plasmas* **10**, 1883–1896.

ZHOU, Y., *et al.* 2021 Rayleigh–Taylor and Richtmyer–Meshkov instabilities: a journey through scales. *Physica D* **423**, 132838.